Computer Methods in Applied Mechanics and Engineering 447 (2025) 118350

Contents lists available at ScienceDirect

Comput. Methods Appl. Mech. Engrg.

journal homepage: www.elsevier.com/locate/cma

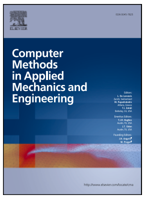

Peridynamic correspondence model for nearly-incompressible finite elasticity

Francesco Scabbia [a], Vito Diana [b,*], Francesca Fantoni [c], Mirco Zaccariotto [a], Ugo Galvanetto [a]

[a] *Department of Industrial Engineering, University of Padova, Padua, Italy*
[b] *Department of Civil, Chemical and Environmental Engineering, University of Genova, Genoa, Italy*
[c] *Department of Civil, Environmental, Architectural Engineering and Mathematics, Università degli Studi di Brescia, Brescia, Italy*

ARTICLE INFO

Keywords:
State-based models
Hyperelasticity
Large deformations
Elastomers
Soft tissues

ABSTRACT

This paper presents a correspondence model for use with peridynamic states in the context of nearly incompressible finite elasticity. An isochoric/volumetric decomposition is adopted, enabling the derivation of the peridynamic force state from a purely spherical, pointwise non-local deformation gradient and a deviatoric, bond-level non-local deformation gradient. This approach leads to a stable one-field, state-based peridynamic formulation that is free from zero-energy modes and capable of accurately capturing the mechanical behavior of elastic materials under large deformations, including those with low or negligible compressibility, typical of unfilled elastomers and isotropic soft biological tissues. Notably, the proposed correspondence model, based on a selective bond-associated deformation gradient, avoids the artificial stiffening commonly observed in standard displacement-based formulations near the incompressible limit. Moreover, its performance is shown to be independent of the specific compressibility ratio assumed in the hyperelastic constitutive law. The model has been successfully validated using classical polynomial strain energy functions through a series of illustrative examples involving both homogeneous and inhomogeneous finite deformations in isotropic hyperelastic solids.

1. Introduction

Hyperelastic materials, such as filled and unfilled elastomers used in advanced industrial engineering [1–3] or soft tissues present in biomechanics [4,5], have been extensively investigated for their important practical applications. Hyperelastic materials are characterized by non-linear constitutive and kinematic models [6,7], which makes them challenging to be analyzed in the context of computational mechanics. Moreover, some applications include the presence of discontinuities, such as fracture in elastomers and cuts in biological tissues. Mesh-based models have been used to simulate hyperelastic materials with evolving discontinuities (see, for instance, [8,9]), but the distortion of the elements due to large deformations may lead to the necessity of remeshing [10]. Furthermore, models based on classical continuum mechanics are not directly suitable for problems involving discontinuities, as they rely on partial derivatives of the displacement field. On the other hand, problems with evolving discontinuities can be naturally analyzed using theories that do not include spatial derivatives in their formulation, such as peridynamics [11,12], a nonlocal continuum theory specifically devised to model discontinuities without mathematical inconsistencies. In fact, peridynamic theory reformulates the

---

[*] Corresponding author.
E-mail address: vito.diana@unige.it (V. Diana).

https://doi.org/10.1016/j.cma.2025.118350
Received 10 June 2025; Received in revised form 25 July 2025; Accepted 25 August 2025

equations of motion of classical continuum mechanics in terms of integro-differential equations, which remain valid in the presence of discontinuities in the displacement field. In a peridynamic body, material points interact through *bonds* over a finite distance, referred to as the *horizon*. Different versions of the theory arise depending on the specific definition of the bond forces.

In bond-based peridynamics [11], the bond forces are always aligned to the bond and are derived from a pairwise function. In this version of the theory, Poisson's ratio is limited to a fixed value due to Cauchy's relations [13,14]. Nevertheless, some constitutive models for hyperelastic materials have been included in bond-based peridynamics. Silling and Bobaru [15] proposed a bond-based model for hyperelastic compressible materials with a strain energy density equivalent to a special case of the Blatz-Ko model. The bond forces for a Neo-Hookean, incompressible, bond-based peridynamic material under homogeneous deformations were computed in [16]. The constitutive model for the bond forces was calibrated directly with experimental observations in [17], while a physically-based peridynamic model for polymers was proposed in [18]. Other examples of hyperelatic materials modeled with bond-based peridynamics can be found, among others, in [19,20]. However, the capabilities of including general hyperelastic constitutive models into bond-based peridynamics are rather limited at the state of the art [21]. In state-based peridynamics [12], the bond forces are determined through a multi-body potential function, which allows to avoid the limitation on the fixed Poisson's ratio in isotropic materials. In ordinary state-based peridynamics, bond forces are aligned with the bond direction, whereas in non-ordinary state-based peridynamics, bond forces may exhibit a general orientation [12,22]. The most common approach to modeling hyperelastic materials within state-based peridynamics has been through correspondence models (see, among others, [23–32]). Correspondence models operate, in general terms, according to the following procedure: (1) a nonlocal averaged quantity analogous to the deformation gradient is defined; (2) this nonlocal deformation gradient is used in the classical stress-strain constitutive relations to compute a stress tensor; and (3) the resulting stress tensor is then averaged to obtain the force density [33]. Correspondence models based on the definition of the non-local deformation gradient typically lie within the framework of non-ordinary state-based peridynamics [22,34]. Nonetheless, the adoption of strain gradients, as opposed to the deformation gradient, as the auxiliary measure may lead to ordinary-state-based formulations [35,36]. However, such formulations have shown certain material instability effects under homogeneous deformation [37]. In any case, since the deformation gradient tensor is computed through an integral average over the family region, there is generally no one-to-one correspondence between the displacement field and the nonlocal deformation gradient. This may result in nontrivial displacement fields with vanishing nonlocal deformation, and consequently vanishing elastic energy density. For this reason, correspondence models suffer from instability issues in the form of zero-energy modes [35]. Therefore, they require additional stabilization techniques to obtain reasonable numerical results [33,38–40]. For example, penalty methods that tend to reduce deviations of the bond deformation state from bond deformation given by the deformation gradient tensor, such as in [38,39], can be used. However, these methods include some parameters that are not uniquely defined and have to be tuned depending on the chosen model. The authors of [33,40] propose, instead, new bond-level definitions of the peridynamic deformation gradient tensor. While this leads to increased computational time, it also ensures a stable solution of the peridynamic governing equations. Bond-level or bond-associated stabilization techniques have emerged as the prevailing computational strategies for correspondence models within displacement-based formulations of state-based peridynamics [41].

Most elastomers and soft tissues in undrained conditions exhibit negligible compressibility characteristics, with equivalent Poisson's ratios close to $1/2$. Displacement-based formulations for nearly-incompressible elasticity may suffer from numerical instabilities and the well-known issue of *volumetric locking*, that is, an overly stiff behavior near the incompressibility limit, which compromises the correct prediction of the elastic energy stored in the system. This issue generally affects displacement-based formulations in mechanics, such as those obtained through approximation techniques like the finite element method, especially in the case of linear displacement field approximations [42]. Correspondence models adopted in the literature to simulate hyperelastic materials have been tested almost exclusively either for materials with a significant degree of compressibility [23,27,30,32], or under plane stress conditions [24,25,29,31], for which, notoriously, one-field computational formulations in solid mechanics do not exhibit istabilities related to the ill-contitioning of the tangent stiffness matrix when approaching the incompressible limit. This paper highlights that, under plane strain conditions, bond-associated correspondence models discretized according to classical meshfree approaches (e.g., piecewise-constant displacement field approximations) may exhibit an overly stiff response and fail to accurately reproduce the strain energy density of nearly incompressible elastic materials. This behavior is, to some extent, analogous to the volumetric locking phenomenon commonly observed in single-field formulations derived from classical continuum mechanics, such as those employed in standard finite element approximations. In the broader context of the peridynamic literature, the incompressibility condition has been addressed by Bode et al., who proposed a mixed displacement-pressure-dilation formulation based on interpolating moving least square shape functions [43]. In their approach, the governing equations of the discretized system are derived using multi-field variational principles. Hence, the objective of this paper is to propose an effective method to address the problem of locking phenomena in correspondence models based on bond-associated deformation gradients, namely the selective bond-associated correspondence model. The proposed approach preserves the formal structure of the displacement-based formulation of state-based peridynamics, which is obtained through direct discretization of the strong-form integro-differential field equations, in line with the classical meshfree approach [41,44]. In particular, an isochoric/volumetric decomposition is employed, allowing the peridynamic force state to be derived from a purely spherical, pointwise nonlocal deformation gradient and a deviatoric, bond-level nonlocal counterpart. This formulation results in a stable, one-field, state-based peridynamic model that avoids zero-energy modes and accurately captures the mechanical response of elastic materials undergoing large deformations, including nearly incompressible behavior typically observed in rubber-like materials and soft biological tissues. These results support the prediction through peridynamic correspondence models and classical hyperelastic constitutive laws of fracture in elastomeric materials and cuts in soft biological tissues.

The paper is structured as follows. Section 2 provides an overview of the constitutive laws of classical continuum mechanics for hyperelastic nearly-incompressible materials, the original version of the correspondence model with non-ordinary state-based peridynamics [12], and the bond-associated stabilization approach [40]. Section 3 presents the approach proposed to address the locking-type issues in bond-associated correspondence models for nearly incompressible materials. Section 4 presents numerical results from several examples featuring increasingly complex deformation states and varying overall deformation characteristics, aimed at comparing the accuracy of the proposed method with that of the bond-associated correspondence model. Section 5 summarizes the main findings of the study.

2. Finite elasticity and peridynamic correspondence models

This section opens with a concise overview of phenomenological constitutive models for isotropic finite hyperelasticity within the framework of classical continuum mechanics. Subsequently, we show how such constitutive equations can be embedded into the (non-ordinary) state-based peridynamic formulation through the use of correspondence models. Stabilization strategies-commonly adopted to eliminate zero-energy modes in correspondence material models [45]-are also addressed, along with the discretization of the peridynamic equations via a meshfree approach [44].

2.1. *Hyperelastic strain-energy functions: constitutive equations in terms of invariants*

Hyperelastic materials here considered postulate the existence of a free-energy function of the form $\psi = \psi(\mathbf{F})$, with $\mathbf{F}$ being the deformation gradient [46]. Making use of the representation theorem for invariants [47], free energy functions (i.e. strain-energy functions or stored energy functions) for a material that withstands material objectivity and isotropy can be expressed-considering material description-as a set of independent invariants $I_1(\mathbf{C})$, $I_2(\mathbf{C})$, and $I_3(\mathbf{C})$ of the right Cauchy-Green strain tensor $\mathbf{C} = \mathbf{F}^\top\mathbf{F}$, namely $\psi = \psi\left(I_1(\mathbf{C}), I_2(\mathbf{C}), I_3(\mathbf{C})\right)$. When minimal volumetric deformations are observed even at highly strained states, the material may be regarded as incompressible so that only isochoric motions are possible. In this case, the hyperelastic material is characterized by the incompressibility constraint $J \equiv \det\mathbf{F} = 1$, and consequently, $I_3 \equiv \det(\mathbf{C}) = 1$. This assumption is commonly accepted for several elastic materials, particularly in the modeling of unfilled elastomers and soft biological tissues, where the nearly incompressible behavior arises from their biphasic nature-specifically, the high water content and the rapid application of external loads [4]. The strain energy function can then be written, in a general form, as $\psi = \psi(\mathbf{F}) - p(J-1)$ where the scalar p serves as an indeterminate Lagrange multiplier, which can be identified as a hydrostatic pressure [46]. Actually, in the incompressible case, the hyperelastic constitutive law allows the determination of only the stress deviator, while the hydrostatic pressure is recovered from equilibrium and boundary conditions.

In the context of computational mechanics, the incompressibility constraint is often addressed through a *compressible regularization* approach. This approach, which conveniently preserves the use of one-field variational principles, is based on the physical idea of modeling an incompressible material as slightly compressible by assigning a large value to the bulk modulus [46,48]. By resorting the concept of deviatoric and volumetric multiplicative split of the deformation gradient $\mathbf{F} = \mathbf{F}_{\text{dev}}\mathbf{F}_{\text{vol}}$ with $\mathbf{F}_{\text{dev}} = J^{-\frac{1}{3}}\mathbf{F}$ and $\mathbf{F}_{\text{vol}} = J^{\frac{1}{3}}\mathbf{I}$, the deviatoric component of the right Cauchy-Green strain tensor reads

$$\mathbf{C}_{\text{dev}} \equiv \mathbf{F}_{\text{dev}}^\top\mathbf{F}_{\text{dev}} = J^{-\frac{2}{3}}\mathbf{F}^\top\mathbf{F}\,. \tag{1}$$

The strain energy function is thus additively decomposed into a deviatoric and a purely volumetric contribution as

$$\psi = \psi_{\text{dev}} + \psi_{\text{vol}}\,, \tag{2}$$

where ψ_{dev} depends on the deviatoric part of the right Cauchy-Green deformation tensor, $\mathbf{C}_{\text{dev}}$, and ψ_{vol} is a function of J, typically motivated by mathematical considerations to enforce near-incompressibility. This contribution is commonly referred to as a penalty function, and it often takes the simple form

$$\psi_{\text{vol}} = \frac{1}{2}\kappa(J-1)^2, \tag{3}$$

which is widely used in numerical computations [48–51]. Here, $\kappa > 0$ denotes the bulk modulus, which characterizes the relationship between hydrostatic pressure and the volumetric part of the deformation gradient, $\mathbf{F}_{\text{vol}}$.

The volume-preserving or distortional part of the strain energy function may be assumed, for instance, as the regularized version of the Mooney-Rivlin energy potential, which can be written as [52]

$$\psi_{\text{dev}} = C_1\left(I_1^* - 3\right) + C_2\left(I_2^* - 3\right), \tag{4}$$

where I_1^* and I_2^* are the principal invariants of $\mathbf{C}_{\text{dev}}$, while $\mu = 2(C_1 + C_2)$ is the initial shear modulus. From Eq. (4), the Neo-Hookean strain energy function is recovered as a special case by setting $C_2 = 0$, leading to

$$\psi_{\text{dev}} = \frac{1}{2}\mu\left(I_1^* - 3\right). \tag{5}$$

It is worth noting that, when $\kappa \to +\infty$, the incompressible limit ($J = 1$) is approached. Therefore, it should be underlined that ψ_{vol} represents a penalty contribution to the strain energy function, with the bulk modulus κ playing the role of a penalty factor that penalizes, in fact, volumetric deformations. This is a standard methodology for computationally handling the constraint $J = 1$ [53]. Another consideration is that the penalty function ψ_{vol} (i.e. the volumetric contribution to the strain energy density) may assume different forms with respect to the expression in Eq. 3 [54–57]. For example $\psi_{\text{vol}} = \varsigma\kappa(\ln J)^2$ with $\varsigma = 1/2$ is also frequently employed for nearly incompressible material models [48,50]. This also applies to the distortional part of the strain energy function, which can also be expressed in a generalized polynomial form [52]. Without loss of generality, in this work we consider the volumetric energy as given in Eq. (3), and adopt Eqs. (4) and (5) for the deviatoric contribution.

The second Piola-Kirchhoff stress tensor can be determined by differentiating the hyperelastic strain energy density with respect to the strain tensor. In the case of a nearly-incompressible Mooney-Rivlin strain energy density, the second Piola-Kirchhoff stress tensor becomes [51]

$$\mathbf{S} = 2\frac{\partial \psi}{\partial \mathbf{C}} = 2\left(C_1 \frac{\partial I_1^*}{\partial \mathbf{C}} + C_2 \frac{\partial I_2^*}{\partial \mathbf{C}} + \kappa (J-1) \frac{\partial J}{\partial \mathbf{C}} \right). \tag{6}$$

Similarly, the elasticity tensor can be computed by differentiating the second Piola-Kirchhoff stress tensor [51]:

$$\mathbb{D} = 2\frac{\partial \mathbf{S}}{\partial \mathbf{C}} = 4\left(C_1 \frac{\partial^2 I_1^*}{\partial \mathbf{C}^2} + C_2 \frac{\partial^2 I_2^*}{\partial \mathbf{C}^2} + \kappa \frac{\partial J}{\partial \mathbf{C}} \otimes \frac{\partial J}{\partial \mathbf{C}} + \kappa (J-1) \frac{\partial^2 J}{\partial \mathbf{C}^2} \right). \tag{7}$$

These equations are employed in the non-linear analysis to compute the internal force vector and the tangent stiffness matrix associated with the discretized mechanical model, as detailed in Section 3.2.

At this point, it is important to note that, from a numerical perspective, instability phenomena such as divergence and volumetric locking-i.e., the occurrence of spurious overly stiff solutions-may arise in one-field formulations of discretized classical continuum mechanics problems as the incompressible limit is approached. For instance, in the finite element method, this issue arises from the inability of low-order interpolation polynomials to accurately capture general volume-preserving displacement fields. As a result, the tangent stiffness matrix becomes increasingly ill-conditioned for increasing bulk modulus κ. Nevertheless, due to their computational efficiency and simplicity, low-order elements are often preferred in large-scale simulations. To enable their effective use near the incompressible limit, several alternative formulations and stabilization techniques have been proposed in the literature [42,52], as reviewed at the beginning of Section 3.

2.2. *Peridynamic correspondence models*

Correspondence models are devised to embed the (possibly complex) phenomenological constitutive laws of classical continuum mechanics into a (state-based type) peridynamic framework. The fundamental idea underlying these models is to define a nonlocal, averaged quantity analogous to the deformation gradient $\mathbf{F}$. This second-order tensor is then employed within classical continuum stress-deformation relationships to compute a local stress tensor, which is subsequently averaged to determine the peridynamic force density [22]. In other words, $\mathbf{F}$ can be replaced by the peridynamic deformation gradient tensor, denoted by $\overline{\mathbf{F}}$, in the constitutive relations of classical continuum mechanics.

Let us denote the bond vector between two points $\mathbf{x}$ and $\mathbf{x}'$ in the reference (initial) configuration by $\boldsymbol{\xi} = \mathbf{x}' - \mathbf{x}$, and the deformed bond vector by $\underline{\mathbf{Y}}\langle\boldsymbol{\xi}\rangle = \mathbf{y}' - \mathbf{y}$, where $\mathbf{y}$ and $\mathbf{y}'$ are the positions of the points $\mathbf{x}$ and $\mathbf{x}'$ in the deformed configuration, respectively. $\underline{\mathbf{Y}}$ is the deformation vector state. As usual in the peridynamic community, an underlined tensor-, vector- or scalar-valued variable indicates a state, while the angle bracket notation indicates that the state is associated with bond $\boldsymbol{\xi}$. The relative displacement of the bond is given by the displacement vector state $\underline{\mathbf{U}}\langle\boldsymbol{\xi}\rangle = \mathbf{u}' - \mathbf{u}$, where $\mathbf{u}$ and $\mathbf{u}'$ are the displacement vectors of the points $\mathbf{x}$ and $\mathbf{x}'$, respectively. The mutual relations among $\boldsymbol{\xi}$, $\underline{\mathbf{Y}}\langle\boldsymbol{\xi}\rangle$, and $\underline{\mathbf{U}}\langle\boldsymbol{\xi}\rangle$, are shown in Fig. 1.

The non-local deformation gradient (namely the peridynamic deformation gradient tensor) at $\mathbf{x}$ is defined as [12]

$$\overline{\mathbf{F}}(\mathbf{x}) = \left(\int_{\mathcal{H}_{\mathbf{x}}} \underline{\omega}\langle\boldsymbol{\xi}\rangle\, \underline{\mathbf{Y}}\langle\boldsymbol{\xi}\rangle \otimes \boldsymbol{\xi}\, \mathrm{d}V_{\mathbf{x}'} \right) \left(\overline{\mathbf{K}}(\mathbf{x}) \right)^{-1}, \tag{8}$$

where $\mathcal{H}_{\mathbf{x}}$ is the integration region around point $\mathbf{x}$, $\underline{\omega}\langle\boldsymbol{\xi}\rangle$ is the influence function, $\mathrm{d}V_{\mathbf{x}'}$ is the infinitesimal volume of a point $\mathbf{x}'$ within $\mathcal{H}_{\mathbf{x}}$, and $\overline{\mathbf{K}}(\mathbf{x})$ is the shape tensor. The integration region $\mathcal{H}_{\mathbf{x}}$, knows as the *neighborhood* of $\mathbf{x}$, is often chosen to be a circle in 2D and a sphere in 3D, with a radius δ, named *horizon size*, such that $\mathcal{H}_{\mathbf{x}} = \left\{ \mathbf{x}' \in \mathcal{B}(t=0) : \|\boldsymbol{\xi}\| \leq \delta \right\}$. In this work, the exponential influence function is adopted, namely $\underline{\omega}\langle\boldsymbol{\xi}\rangle = \underline{\hat{\omega}}\langle\boldsymbol{\xi}\rangle = \exp(-\|\boldsymbol{\xi}\|^2/\delta^2)$ [58]. The shape tensor is given as

$$\overline{\mathbf{K}}(\mathbf{x}) = \int_{\mathcal{H}_{\mathbf{x}}} \underline{\omega}\langle\boldsymbol{\xi}\rangle\, \boldsymbol{\xi} \otimes \boldsymbol{\xi}\, \mathrm{d}V_{\mathbf{x}'} . \tag{9}$$

Note that, for a homogeneous deformation $\mathbf{F}_0$, the deformation vector state becomes $\underline{\mathbf{Y}}\langle\boldsymbol{\xi}\rangle = \mathbf{F}_0\, \boldsymbol{\xi}$, and therefore, from Eq. (8), $\overline{\mathbf{F}} = \mathbf{F}_0$.

Eq. (8) defines the peridynamic counterpart of the classical deformation gradient tensor. In fact, $\overline{\mathbf{F}}$ can be substituted for $\mathbf{F}$ in any constitutive law of classical continuum mechanics. For instance, $\overline{\mathbf{F}}$ can be used to compute the quantities in all the equations of Sections 2.1. As in a model based on classical continuum mechanics, the second Piola-Kirchhoff stress tensor $\mathbf{S}$ can be computed by deriving the strain energy density of the considered material with respect to the deformation gradient tensor, as shown, for example, in Eq. (6). The first Piola-Kirchhoff stress tensor can then be obtained as $\overline{\mathbf{P}} = \mathbf{P}(\overline{\mathbf{F}}) = \overline{\mathbf{F}}\, \overline{\mathbf{S}}$.

The integro-differential state-based peridynamic equation of motion is given by [12]:

$$\rho(\mathbf{x})\, \ddot{\mathbf{u}}(\mathbf{x},t) - \int_{\mathcal{H}_{\mathbf{x}}} \left(\underline{\mathbf{T}}[\mathbf{x},t]\langle\boldsymbol{\xi}\rangle - \underline{\mathbf{T}}[\mathbf{x}',t]\langle-\boldsymbol{\xi}\rangle \right) \mathrm{d}V_{\mathbf{x}'} = \mathbf{b}(\mathbf{x},t), \tag{10}$$

where ρ is the density of the material, $\ddot{\mathbf{u}}$ is the acceleration field, $\underline{\mathbf{T}}$ is the force state (force per unit volume squared), and $\mathbf{b}$ is the external force density. In non-ordinary state-based peridynamics, the force state is not necessarily aligned with the bond direction,

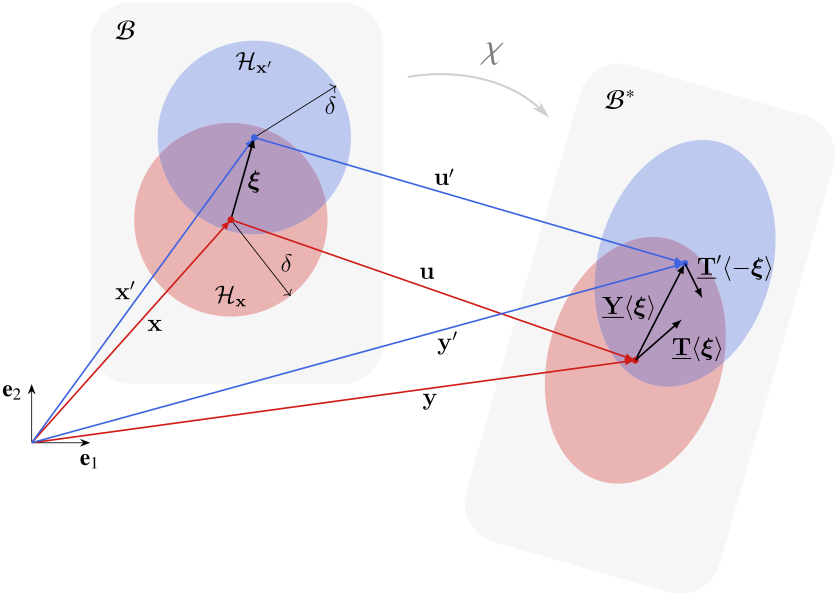

Fig. 1. Detail of the reference configuration $\mathcal{B}$ and deformed configuration $\mathcal{B}^*$ of a state-based peridynamic continuum domain.

as shown in Fig. 1. The force state is computed as [12]

$$\underline{\overline{\mathbf{T}}}[\mathbf{x},t]\langle\xi\rangle = \underline{\omega}\langle\xi\rangle\,\overline{\mathbf{P}}(\mathbf{x})\Big(\overline{\mathbf{K}}(\mathbf{x})\Big)^{-1}\xi\,, \tag{11}$$

where square brackets are used for peridynamic states with the same meaning as standard parentheses, indicating dependence on quantities. Therefore, the force state $\underline{\mathbf{T}}$ incorporates the classical constitutive law through the stress tensor $\overline{\mathbf{P}}$, which depends upon the peridynamic deformation gradient tensor $\overline{\mathbf{F}}$, thus establishing a direct connection between the constitutive models of classical continuum mechanics and peridynamics.

In bond-based peridynamics, the generalized force interaction between two material points depends explicitly and exclusively on the deformation of the bond connecting them, consistent with a pairwise interaction formalism. In state-based peridynamic formulations, the force interaction is derived from the peridynamic force state, which depends on the collective deformation of all bonds within the neighborhoods of the interacting material points, as characterized by the peridynamic deformation state $\underline{\mathbf{Y}}$. In correspondence models, deformations contained in the force state are represented by the non-local deformation gradient $\overline{\mathbf{F}}$, which amounts to approximating the bond deformations by the first term in a Taylor series centered at $\mathbf{x}$ [22](see Eq. (8)). However, the correspondence model suffers from non-invertibility, which reflects an underlying material instability rather than being merely an artifact of meshless discretization [40]. Actually, correspondence models allow for multiple displacement fields within a neighborhood to lead to the same deformation gradient tensor [33]. Thus, in the solution of a boundary value problem, so-called zero-energy mode instabilities may appear for materials modeled with a non-ordinary state-based formulation derived using correspondence models.

Several methods have been developed to eliminate these instabilities from correspondence models, but most of them rely on one of the following two main approaches. The first approach is based on penalty methods that tend to reduce deviations of the bond deformation state from $\overline{\mathbf{F}}$, such as in [38,39]. The second approach is based on the use of a different definition of the non-local deformation gradient tensor. For instance, the stabilization method proposed by Breitzman and Dayal [33], termed here the *bond-level correspondence model*, defines a peridynamic deformation gradient tensor with an additional term that is related to a bond rather than a point. The stabilization method proposed by Chen [40], knows as the *bond-associated correspondence model*, modifies the integration regions of the integrals of Eqs. (8) and (9), so that the peridynamics deformation gradient tensor is uniquely defined for each bond. The latter stabilization methods-which in fact constitute the standard computational schemes for peridynamic correspondence models-replace the conventional pointwise-defined nonlocal deformation gradient with specifically defined bond-level nonlocal deformation gradients. That said, the procedure described in [40] is the most widely adopted stabilization method for correspondence models in the literature, and it will be examined in detail in the following paragraph.

2.2.1. Bond-associated deformation gradients

The bond-associated correspondence model makes use of a simple and effective modification of the peridynamic deformation gradient tensor in Eq. 8 to provide a bond-level definition of the non-local deformation gradient [40]. Actually, the bond-associated deformation gradient tensor, denoted by $\widetilde{\mathbf{F}}$, is defined as [40,45]

$$\widetilde{\mathbf{F}}(\xi) = \left(\int_{\mathcal{H}_{\mathbf{x}}\cap\mathcal{H}_{\mathbf{x}'}} \underline{\omega}\langle\xi\rangle\,\underline{\mathbf{Y}}\langle\xi\rangle\otimes\xi\,\mathrm{d}V_{\mathbf{x}'}\right)\Big(\widetilde{\mathbf{K}}(\xi)\Big)^{-1}, \tag{12}$$

where $\boldsymbol{\xi}$ is the bond between points $\mathbf{x}$ and $\mathbf{x}'$ and the bond-associated shape tensor is similarly given as

$$\widetilde{\mathbf{K}}(\boldsymbol{\xi}) = \int_{\mathcal{H}_{\mathbf{x}}\cap\mathcal{H}_{\mathbf{x}'}} \underline{\omega}\langle\boldsymbol{\xi}\rangle\,\boldsymbol{\xi}\otimes\boldsymbol{\xi}\,\mathrm{d}V_{\mathbf{x}'}\,. \tag{13}$$

Note that the difference between the deformation gradient tensor $\overline{\mathbf{F}}$ and the bond-associated tensor $\widetilde{\mathbf{F}}$ relies in the integration region of the two corresponding integrals. The integration region of the bond-associated deformation gradient tensor is the intersection between the neighborhoods of the nodes connected by the bond. This integration region is shown in Fig. 1 with a purplish color. The original bond-associated stabilization method proposes that the horizon size associated with the neighboring point $\mathbf{x}'$ could also assume different values, but choosing the same value of δ provides small errors and a linear convergence rate [59]. This also reduces the computational cost and the memory allocation of the numerical simulations in discretized systems, without mentioning the great advantage of reducing the number of parameters of the model.

The bond-associated force state is computed as [40,45]

$$\widetilde{\underline{\mathbf{T}}}[\mathbf{x},t]\langle\boldsymbol{\xi}\rangle = \frac{\int_{\mathcal{H}_{\mathbf{x}}\cap\mathcal{H}_{\mathbf{x}'}}\mathrm{d}V_{\mathbf{x}'}}{\int_{\mathcal{H}_{\mathbf{x}}}\mathrm{d}V_{\mathbf{x}'}}\,\underline{\omega}\langle\boldsymbol{\xi}\rangle\,\widetilde{\mathbf{P}}(\boldsymbol{\xi})\Big(\widetilde{\mathbf{K}}(\boldsymbol{\xi})\Big)^{-1}\boldsymbol{\xi}\,, \tag{14}$$

where $\widetilde{\mathbf{P}} = \mathbf{P}(\widetilde{\mathbf{F}}) = \widetilde{\mathbf{F}}\,\widetilde{\mathbf{S}}$ is the bond-associated first Piola-Kirchhoff stress tensor, that can be computed, for example, from Eq. (6). This tensor is computed by means of the constitutive laws of classical continuum mechanics in which the deformation gradient tensor is $\widetilde{\mathbf{F}}$. Being the bond-associated deformation gradient tensor uniquely defined for each bond, the bond-associated force state of a bond depends on a deformation measure associated to that bond and the zero-energy mode instabilities vanish.

The peridynamic equation of motion for the bond-associated stabilization method reads

$$\rho(\mathbf{x})\,\ddot{\mathbf{u}}(\mathbf{x},t) - \int_{\mathcal{H}_{\mathbf{x}}}\Big(\widetilde{\underline{\mathbf{T}}}[\mathbf{x},t]\langle\boldsymbol{\xi}\rangle - \widetilde{\underline{\mathbf{T}}}[\mathbf{x}',t]\langle-\boldsymbol{\xi}\rangle\Big)\,\mathrm{d}V_{\mathbf{x}'} = \mathbf{b}(\mathbf{x},t)\,. \tag{15}$$

The numerical implementation of this method, based on a meshfree approach, is reported hereinafter.

2.3. Numerical implementation

To discretize a body modeled by the stabilized correspondence model, we employ the standard node-based meshfree method with uniform grid spacing Δx [44] (see Fig. 2), which is the most widely used discretization method in the peridynamic literature. According to this method, each node is associated with a subdomain of area Δx^2 of the 2D body.

The deformation gradient tensor (in the original version of the non-ordinary state-based formulation) for a node $\mathbf{x}_i$ can be computed in the discretized model as

$$\overline{\mathbf{F}}_i = \overline{\mathbf{F}}(\mathbf{x}_i) = \left(\sum_{k\in\mathcal{H}_i}\underline{\omega}\langle\boldsymbol{\xi}_{ik}\rangle\,\underline{\mathbf{Y}}\langle\boldsymbol{\xi}_{ik}\rangle\otimes\boldsymbol{\xi}_{ik}\,\beta_{ik}\Delta V\right)\Big(\overline{\mathbf{K}}_i\Big)^{-1}, \tag{16}$$

where $\boldsymbol{\xi}_{ik} = \mathbf{x}_k - \mathbf{x}_i$, the deformed bond vector is given as $\underline{\mathbf{Y}}\langle\boldsymbol{\xi}_{ik}\rangle = \boldsymbol{\xi}_{ik} + \mathbf{u}_k - \mathbf{u}_i$ with $\mathbf{u}_i = \mathbf{u}(\mathbf{x}_i)$ and $\mathbf{u}_k = \mathbf{u}(\mathbf{x}_k)$, and the shape tensor reads

$$\overline{\mathbf{K}}_i = \overline{\mathbf{K}}(\mathbf{x}_i) = \sum_{k\in\mathcal{H}_i}\underline{\omega}\langle\boldsymbol{\xi}_{ik}\rangle\,\boldsymbol{\xi}_{ik}\otimes\boldsymbol{\xi}_{ik}\,\beta_{ik}\Delta V\,. \tag{17}$$

The volume associated with each node in a 2D model is $\Delta V = t\,\Delta x^2$, where t is the thickness of the body. Furthermore, the quadrature coefficient β_{ik} is introduced in Eqs. (16) and (17) in order to improve the accuracy of the numerical integration. β_{ik} represents the fraction of the area of node k lying within the neighborhood of node i, as shown in Fig. 2, and we use the algorithm developed in [60] to compute it. Therefore, the nodes used in the summations (with index k) are the nodes with a portion of their volume lying within

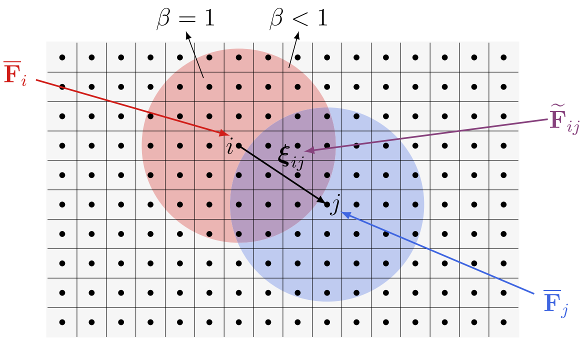

Fig. 2. Discretization of the peridynamic body using a meshfree method with uniform grid spacing. The nodes within the red and blue regions are used in the formulae to compute the deformation gradient tensor in the original formulation for nodes i and j, respectively, whereas the nodes in the purplish region are used to compute the bond-associated deformation gradient tensor.

the neighborhood $\mathcal{H}_i$ of node i. The peridynamic equation of motion for a node i in the original correspondence model discretized with the meshfree method is given (multiplying left- and right-hand side by ΔV) as

$$\rho(\mathbf{x}_i)\,\ddot{\mathbf{u}}(\mathbf{x}_i,t)\,\Delta V - \sum_{j\in\mathcal{H}_i}\left(\underline{\overline{\mathbf{T}}}[\mathbf{x}_i,t]\langle\boldsymbol{\xi}_{ij}\rangle - \underline{\overline{\mathbf{T}}}[\mathbf{x}_j,t]\langle\boldsymbol{\xi}_{ji}\rangle\right)\beta_{ij}\,\Delta V^2 = \mathbf{b}(\mathbf{x}_i,t)\,\Delta V\,, \tag{18}$$

where the force state is computed as

$$\underline{\overline{\mathbf{T}}}[\mathbf{x}_i,t]\langle\boldsymbol{\xi}_{ij}\rangle = \underline{\omega}\langle\boldsymbol{\xi}_{ij}\rangle\,\overline{\mathbf{P}}_i\left(\overline{\mathbf{K}}_i\right)^{-1}\boldsymbol{\xi}_{ij}\,, \tag{19}$$

where $\overline{\mathbf{P}}_i = \overline{\mathbf{P}}(\mathbf{x}_i)$ is the first Piola-Kirchhoff stress tensor computed as a function of the deformation gradient tensor given in Eq. (16).

The stabilized version of the discretized correspondence model, namely the bond-associated correspondence model, employs similar formulae obtained by modifying the nodes involved in the summations. The bond-associated deformation gradient tensor for bond $\boldsymbol{\xi}_{ij}$ connecting node i to node j can be computed as

$$\widetilde{\mathbf{F}}_{ij} = \widetilde{\mathbf{F}}(\boldsymbol{\xi}_{ij}) = \left(\sum_{k\in(\mathcal{H}_i\cap\mathcal{H}_j)}\underline{\omega}\langle\boldsymbol{\xi}_{ik}\rangle\,\underline{\mathbf{Y}}\langle\boldsymbol{\xi}_{ik}\rangle\otimes\boldsymbol{\xi}_{ik}\,\beta_{ik}\Delta V\right)\left(\widetilde{\mathbf{K}}_{ij}\right)^{-1}, \tag{20}$$

where the deformed bond vector is given as $\underline{\mathbf{Y}}\langle\boldsymbol{\xi}_{ik}\rangle = \boldsymbol{\xi}_{ik} + \mathbf{u}_k - \mathbf{u}_i$ and the bond-associated shape tensor as

$$\widetilde{\mathbf{K}}_{ij} = \widetilde{\mathbf{K}}(\boldsymbol{\xi}_{ij}) = \sum_{k\in(\mathcal{H}_i\cap\mathcal{H}_j)}\underline{\omega}\langle\boldsymbol{\xi}_{ik}\rangle\,\boldsymbol{\xi}_{ik}\otimes\boldsymbol{\xi}_{ik}\,\beta_{ik}\Delta V\,. \tag{21}$$

In this case, the nodes used in the summations (with index k) are the nodes shared between the neighborhoods $\mathcal{H}_i$ and $\mathcal{H}_j$ of nodes i and j, respectively. The peridynamic equation of motion for a node i in a bond-associated correspondence model is given (multiplying left- and right-hand side by ΔV) as

$$\rho(\mathbf{x}_i)\,\ddot{\mathbf{u}}(\mathbf{x}_i,t)\,\Delta V - \sum_{j\in\mathcal{H}_i}\left(\underline{\widetilde{\mathbf{T}}}[\mathbf{x}_i,t]\langle\boldsymbol{\xi}_{ij}\rangle - \underline{\widetilde{\mathbf{T}}}[\mathbf{x}_j,t]\langle\boldsymbol{\xi}_{ji}\rangle\right)\beta_{ij}\,\Delta V^2 = \mathbf{b}(\mathbf{x}_i,t)\,\Delta V\,, \tag{22}$$

where the bond-associated force state is computed as

$$\underline{\widetilde{\mathbf{T}}}[\mathbf{x}_i,t]\langle\boldsymbol{\xi}_{ij}\rangle = \frac{N_{ij}}{N_i}\,\underline{\omega}\langle\boldsymbol{\xi}_{ij}\rangle\,\widetilde{\mathbf{P}}_{ij}\left(\widetilde{\mathbf{K}}_{ij}\right)^{-1}\boldsymbol{\xi}_{ij}\,, \tag{23}$$

with N_i and N_{ij} the numbers of nodes with a portion of area lying within the neighborhood $\mathcal{H}_i$ of node i and the intersection $\mathcal{H}_i\cap\mathcal{H}_j$ of the neighborhoods of nodes i and j, respectively, and $\widetilde{\mathbf{P}}_{ij} = \widetilde{\mathbf{P}}(\boldsymbol{\xi}_{ij})$ the first Piola-Kirchhoff stress tensor computed as a function of the bond-associated deformation gradient tensor given in Eq. (20).

Since the present work deals with the static solution for non-linear problems of bodies undergoing large deformations, an implicit incremental-iterative solution scheme based on a Newton-Raphson technique has been developed. The details of this scheme are reported in Section 3.2.

An important advantage of correspondence models is that they do not suffer from the peridynamic surface effect. However, the imposition of the boundary conditions in these non-local models is still an open issue. Therefore, the boundary conditions are enforced with approximate techniques. Boundary conditions are here imposed on the most external layer of nodes, as one would do in a local model. It should be noted that, whenever possible, the value of the horizon size δ should be reduced to mitigate the errors arising from the approximations due to the imposition of the boundary conditions.

3. Correspondence models for nearly-incompressible materials

The stabilized correspondence model described in Section 2.3 is capable of accurately solving general inhomogeneous mechanical problems in the case of compressible hyperelastic solids [25]. However, as will be shown in Section 4, the accuracy of the bond-associated correspondence model is markedly sensitive to the material compressibility. Specifically, it is highlighted that correspondence models may exhibit overstiff responses and inaccurately reproduce the strain energy density of the nearly incompressible elastic material, typically when the ratio κ/μ exceeds 2×10^1. This behavior is, to some extent, similar to the volumetric locking phenomenon commonly observed in one-field formulations derived from classical continuum mechanics, such as those employed in standard finite element approximations [42,52]. Actually, in the context of approximation techniques based on classical continuum mechanics, such as the finite element method, several approaches have been proposed to overcome volumetric locking and related numerical instabilities [48]. The simplest one is to use elements of sufficiently high order that can accurately represent the volume-preserving constraint. However, the robustness and simplicity of low-order elements are lost by adopting this approach. Reducing the number of integration points alleviates volumetric locking, but other numerical problems may arise, such as hourglass modes. Mixed variational formulations that introduce the hydrostatic pressure as an independent variable alongside the displacement field, such as the u/p method, have been demonstrated to be effective in the mitigation of volumetric locking [57]. These methods are implemented using hybrid elements, namely finite elements with different interpolation functions for the displacement and pressure fields. An alternative variational approach is the enhanced assumed strain method, which enriches the deformation gradient tensor with an enhanced strain tensor [61]. Another method consists of replacing the deformation gradient tensor with a modified one that is the multiplication of its volumetric part computed at the centroid of the element and its deviatoric part computed at the Gauss points of the elements [48]. This method, based on the selective integration of the volumetric and deviatoric parts of the deformation gradient tensor, is called the F-bar method, and a similar method (the B-bar method) was also proposed for linear analyses [42].

In this section, we then propose, inspired by the F-bar method, a specific correspondence model for nearly-incompressible finite elasticity, which leads to a stable one-field, state-based peridynamic formulation that is free from zero-energy modes and capable of accurately capturing the mechanical behavior of elastic materials under large deformations. The proposed method avoids the need to resort to multi-field variational principles, weak formulations and higher-order approximations of the displacement field, thus allowing the discretized problem to retain a classical displacement-based mathematical formulation. This is consistent with typical node-based meshfree implementations of state-based peridynamics and offers advantages in terms of simplicity and in handling problems involving fracture and (possibly evolving) material discontinuities. Indeed, the use of higher-order displacement/deformation field approximations-through the introduction of reproducing-kernel shape functions [62,63], weak forms and non-linear approximation functions [64–66], or weak forms of the peridynamic equations in combination with peridynamic differential operators [24,25,67] -has the potential to alleviate locking phenomena in displacement-based formulations in the incompressible limit. However, this has not yet been clearly and comprehensively demonstrated, as no applications of the aforementioned models have been presented under actual nearly-incompressible conditions (i.e., values of the bulk-to-shear modulus ratio $\kappa/\mu > 1 \times 10^2$ [49]). In contrast, our approach relies on the direct discretization of the classical strong-form integro-differential peridynamic balance equations using a meshfree method with standard piecewise-constant displacement field approximations.

3.1. Selective bond-associated deformation gradients

We propose a simple method to prevent locking-type phenomena in bond-associated correspondence models. This is done by computing the deviatoric part of the peridynamic deformation gradient tensor with the stabilized version of the correspondence model and the volumetric part with the original correspondence model. The original and bond-associated deformation gradient tensors can be multiplicatively split into their corresponding deviatoric and volumetric parts as follows:

$$\overline{\mathbf{F}}(\mathbf{x}) = \overline{\mathbf{F}}_{\mathrm{dev}}(\mathbf{x})\overline{\mathbf{F}}_{\mathrm{vol}}(\mathbf{x})\,, \tag{24}$$

$$\widetilde{\mathbf{F}}(\boldsymbol{\xi}) = \widetilde{\mathbf{F}}_{\mathrm{dev}}(\boldsymbol{\xi})\widetilde{\mathbf{F}}_{\mathrm{vol}}(\boldsymbol{\xi})\,, \tag{25}$$

where $\overline{\mathbf{F}}$ is the original deformation gradient tensor computed with Eq. (8) and $\widetilde{\mathbf{F}}$ is the bond-associated deformation gradient tensor computed with Eq. (12). Therefore, the peridynamic deformation gradient tensor used to address locking-type issues is given as

$$\widehat{\mathbf{F}}(\boldsymbol{\xi}) = \widetilde{\mathbf{F}}_{\mathrm{dev}}(\boldsymbol{\xi})\overline{\mathbf{F}}_{\mathrm{vol}}(\mathbf{x})\,, \tag{26}$$

where $\widetilde{\mathbf{F}}_{\mathrm{dev}}(\boldsymbol{\xi}) = \widetilde{J}^{-\frac{1}{3}}\widetilde{\mathbf{F}}(\boldsymbol{\xi})$ and $\overline{\mathbf{F}}_{\mathrm{vol}}(\mathbf{x}) = \overline{J}^{\frac{1}{3}}\mathbf{I}$, with $\widetilde{J} = \det \widetilde{\mathbf{F}}(\boldsymbol{\xi})$ and $\overline{J} = \det \overline{\mathbf{F}}(\mathbf{x})$. The new tensor $\widehat{\mathbf{F}}(\boldsymbol{\xi})$ is named *selective bond-associated deformation gradient tensor*. This approach is conceptually related to the selective integration methods used in FEM to mitigate volumetric locking, such as the B-bar or F-bar methods [42,48]. For instance, in a 4-noded quadrilateral finite element the volumetric part of the deformation gradient tensor is computed at the centroid of the element to provide an “averaged” value over the whole element (similar to the volumetric part of the original deformation gradient tensor), whereas the deviatoric part of the deformation gradient tensor is computed at the 4 Gauss points of the fully-integrated element (similar to the deviatoric part of the stabilized deformation gradient tensor).

It is important to note that a peridynamic correspondence model that is based on the selective bond-associated deformation gradient tensor is bound to be stable. In fact, the instabilities due to zero-energy modes are due to the fact that different displacement fields may result in the same deformation gradient tensor. However, this is valid only for the deviatoric part of $\mathbf{F}$, for which a measure of the deformation state associated to each bond is required. The volumetric part of the deformation gradient tensor consists of a scalar value that can be uniquely determined from any displacement field. Therefore, the term $\overline{\mathbf{F}}_{\mathrm{vol}}(\mathbf{x})$ in Eq. (26) does not make unstable a material modeled with the selective bond-associated deformation gradient tensor.

A stabilized correspondence model that alleviates the issue of the volumetric locking is simply obtained by using the newly defined deformation gradient tensor $\widehat{\mathbf{F}}(\boldsymbol{\xi})$ instead of $\overline{\mathbf{F}}(\mathbf{x})$ or $\widetilde{\mathbf{F}}(\boldsymbol{\xi})$. This means that $\widetilde{\mathbf{F}}_{\mathrm{dev}}(\boldsymbol{\xi})$ can be used to compute the deviatoric stress tensor $\widetilde{\mathbf{P}}_{\mathrm{dev}}(\boldsymbol{\xi})$ (with ψ_{dev} determined through, for example, Eq. (4)) and $\overline{\mathbf{F}}_{\mathrm{vol}}(\mathbf{x})$ can be used to compute the volumetric stress tensor $\overline{\mathbf{P}}_{\mathrm{vol}}(\mathbf{x})$ (with ψ_{vol} determined through, for example, Eq. (3)). Therefore, the force state is the sum of the volumetric part of the force state computed from Eq. (11) with the original correspondence model and the deviatoric part of the force state computed from Eq. (14) with the bond-associated correspondence model:

$$\begin{aligned}\underline{\widehat{\mathbf{T}}}[\mathbf{x},t]\langle\boldsymbol{\xi}\rangle &= \underline{\overline{\mathbf{T}}}_{\mathrm{vol}}[\mathbf{x},t]\langle\boldsymbol{\xi}\rangle + \underline{\widetilde{\mathbf{T}}}_{\mathrm{dev}}[\mathbf{x},t]\langle\boldsymbol{\xi}\rangle \\ &= \underline{\omega}\langle\boldsymbol{\xi}\rangle\, \overline{\mathbf{P}}_{\mathrm{vol}}(\mathbf{x})\Big(\overline{\mathbf{K}}(\mathbf{x})\Big)^{-1}\boldsymbol{\xi} + \frac{\int_{\mathcal{H}_{\mathbf{x}}\cap\mathcal{H}_{\mathbf{x}'}} 1\,\mathrm{d}V_{\mathbf{x}'}}{\int_{\mathcal{H}_{\mathbf{x}}} 1\,\mathrm{d}V_{\mathbf{x}'}}\,\underline{\omega}\langle\boldsymbol{\xi}\rangle\, \widetilde{\mathbf{P}}_{\mathrm{dev}}(\boldsymbol{\xi})\Big(\widetilde{\mathbf{K}}(\boldsymbol{\xi})\Big)^{-1}\boldsymbol{\xi}\,.\end{aligned} \tag{27}$$

The peridynamic equation of motion for this method reads

$$\rho(\mathbf{x})\,\ddot{\mathbf{u}}(\mathbf{x},t) - \int_{\mathcal{H}_{\mathbf{x}}} \Big(\underline{\widehat{\mathbf{T}}}[\mathbf{x},t]\langle\boldsymbol{\xi}\rangle - \underline{\widehat{\mathbf{T}}}[\mathbf{x}',t]\langle-\boldsymbol{\xi}\rangle\Big)\,\mathrm{d}V_{\mathbf{x}'} = \mathbf{b}(\mathbf{x},t)\,. \tag{28}$$

The discretized version of this equation according to the meshfree method is given as

$$\rho(\mathbf{x}_i)\,\ddot{\mathbf{u}}(\mathbf{x}_i,t)\,\Delta V - \sum_{j\in\mathcal{H}_i} \Big(\underline{\widehat{\mathbf{T}}}[\mathbf{x}_i,t]\langle\boldsymbol{\xi}_{ij}\rangle - \underline{\widehat{\mathbf{T}}}[\mathbf{x}_j,t]\langle\boldsymbol{\xi}_{ji}\rangle\Big)\,\beta_{ij}\,\Delta V^2 = \mathbf{b}(\mathbf{x}_i,t)\,\Delta V\,, \tag{29}$$

with the force state, obtained with the proposed approach from both Eq. (19) and Eq. (23)), which is computed as

$$\underline{\hat{\mathbf{T}}}[\mathbf{x}_i,t]\langle\boldsymbol{\xi}_{ij}\rangle = \underline{\omega}\langle\boldsymbol{\xi}_{ij}\rangle\,\overline{\mathbf{P}}_{\mathrm{vol},i}\left(\overline{\mathbf{K}}_i\right)^{-1}\boldsymbol{\xi}_{ij} + \frac{N_{ij}}{N_i}\,\underline{\omega}\langle\boldsymbol{\xi}_{ij}\rangle\,\widetilde{\mathbf{P}}_{\mathrm{dev},ij}\left(\widetilde{\mathbf{K}}_{ij}\right)^{-1}\boldsymbol{\xi}_{ij}\,, \tag{30}$$

where $\overline{\mathbf{P}}_{\mathrm{vol},i}$ is computed with the volumetric part of the deformation gradient tensor given in Eq. (16), namely $\overline{\mathbf{F}}_{\mathrm{vol},i} = \overline{J}_i^{\frac{1}{3}}\,\mathbf{I}$, and $\widetilde{\mathbf{P}}_{\mathrm{dev},ij}$ is computed with the deviatoric part of the deformation gradient given in Eq. (20), namely $\widetilde{\mathbf{F}}_{\mathrm{dev},ij} = \widetilde{J}^{-\frac{1}{3}}\widetilde{\mathbf{F}}_{ij}$. Therefore, the numerical implementation is a combination of those of the original and bond-associated correspondence model and is presented in the following section.

3.2. Implicit solution scheme

We developed an implicit scheme to solve non-linear problems using peridynamic correspondence models. We hereinafter present the numerical implementation of the proposed approach, which addresses volumetric locking issues in the stabilized correspondence model and reliably reconstructs the elastic energy near the incompressible limit. This approach is essentially a combination of the original correspondence model to compute the volumetric part of the deformation gradient tensor ($\overline{\mathbf{F}}_{\mathrm{vol}}(\mathbf{x})$) and the bond-associated correspondence model to compute the deviatoric part of the deformation gradient tensor ($\widetilde{\mathbf{F}}_{\mathrm{dev}}(\boldsymbol{\xi})$). Therefore, the numerical implementation of the correspondence model adopting the stabilization devised by Chen (used for both the volumetric and deviatoric parts of the deformation gradient tensor) can be easily obtained from the following discussion.

A non-linear analysis can be solved by means of an incremental-iterative method, as explained, for instance, in [51]. In a load-controlled analysis, the load is imposed incrementally and a Newton-Raphson iterative procedure is employed to find the solution (within a user-prescribed tolerance) at each increment. A similar approach applies to a displacement-controlled analysis, in which the constrained values of the displacements are increased incrementally. For the Newton-Raphson procedure, the tangent stiffness matrix and the internal force vector must be computed at each iteration. To this aim, we adopt a numerical algorithm similar to those proposed in [59,68], which is presented in Algorithm 1. The proposed algorithm is based on the computation of the contributions to the stiffness matrix $\mathbf{K}$ and the internal force vector $\mathbf{f}_{\mathrm{int}}$ due to a generic bond $\boldsymbol{\xi}_{ij}$. Then, the same computations are repeated for all the other bonds in the model (including the bond $\boldsymbol{\xi}_{ji}$).

In each iteration, the displacement vector $\mathbf{U}$ from the previous iteration is known, whereas the increment $\Delta\mathbf{U}$ should be determined to obtain the new displacement vector $\mathbf{U}+\Delta\mathbf{U}$. The displacement vector is assembled with odd indexes for the x components and even indexes for the y components such that the x component for node i is $2i-1$ and the y component is $2i$. The first step consists in computing the deformation gradient tensors from Eqs. (16) and (20). Comparing these equations, it can be noted that the only difference for the computation of the deformation gradient tensor between the original and bond-associated correspondence model is the integration region, i.e., the nodes to be considered in the summation. The original and stabilized shape tensors are computed with Eqs. (17) and (21), respectively, and are rearranged as

$$\overline{\mathbf{B}}_i = \begin{bmatrix} \left(\overline{\mathbf{K}}_i\right)^{-1} & \mathbf{0} \\ \mathbf{0} & \left(\overline{\mathbf{K}}_i\right)^{-1} \end{bmatrix}, \qquad \widetilde{\mathbf{B}}_{ij} = \begin{bmatrix} \left(\widetilde{\mathbf{K}}_{ij}\right)^{-1} & \mathbf{0} \\ \mathbf{0} & \left(\widetilde{\mathbf{K}}_{ij}\right)^{-1} \end{bmatrix}, \tag{31}$$

where $\overline{\mathbf{B}}_i$ and $\widetilde{\mathbf{B}}_{ij}$ are 4×4 matrices. We assemble the $4\times 2n$ matrices $\overline{\mathbf{N}}_i$ and $\widetilde{\mathbf{N}}_{ij}$ as shown in Algorithm 1 (lines 5–17) to compute the summation of Eqs. (16) and (20), respectively. n is the total number of nodes in the peridynamic model. The deformation gradient tensors (rearranged in a vector form) can be therefore computed as

$$\overline{\boldsymbol{\mathsf{F}}}_i = \begin{bmatrix} \overline{\mathbf{F}}_i(1,1) \\ \overline{\mathbf{F}}_i(1,2) \\ \overline{\mathbf{F}}_i(2,1) \\ \overline{\mathbf{F}}_i(2,2) \end{bmatrix} = \overline{\mathbf{B}}_i\,\overline{\mathbf{N}}_i\,\mathbf{U} + \boldsymbol{\mathsf{I}}\,, \qquad \widetilde{\boldsymbol{\mathsf{F}}}_{ij} = \begin{bmatrix} \widetilde{\mathbf{F}}_{ij}(1,1) \\ \widetilde{\mathbf{F}}_{ij}(1,2) \\ \widetilde{\mathbf{F}}_{ij}(2,1) \\ \widetilde{\mathbf{F}}_{ij}(2,2) \end{bmatrix} = \widetilde{\mathbf{B}}_{ij}\,\widetilde{\mathbf{N}}_{ij}\,\mathbf{U} + \boldsymbol{\mathsf{I}}\,, \tag{32}$$

where $\mathbf{I}$ is the identity tensor. Note that $\mathbf{F}$ indicates a matrix, whereas $\boldsymbol{\mathsf{F}}$ indicates the same matrix written in a vector form, as shown in Eq. (32).

As proposed in Section 3, we use only the volumetric part of the original deformation gradient tensor, namely $\overline{\mathbf{F}}_{\mathrm{vol},i} = \overline{J}^{-\frac{1}{3}}\,\overline{\mathbf{F}}_i$, and the deviatoric part of the bond-associated deformation gradient tensor, namely $\widetilde{\mathbf{F}}_{\mathrm{dev},ij} = \widetilde{J}^{-\frac{1}{3}}\widetilde{\mathbf{F}}_{ij}$, where $\overline{J} = \det\overline{\mathbf{F}}(\mathbf{x})$ and $\widetilde{J} = \det\widetilde{\mathbf{F}}(\boldsymbol{\xi})$. This simple approach prevents volumetric locking-type problems and ensures accurate reproduction of the elastic energy under near-incompressibility conditions, while formally preserving the standard mathematical structure of discretized non-ordinary state-based peridynamic governing equations. Considering classical continuum mechanics identities (see, for example, Eqs. (6) and (7)), $\overline{\mathbf{F}}_{\mathrm{vol},i}$ and $\widetilde{\mathbf{F}}_{\mathrm{dev},ij}$ can be used to obtain the corresponding second Piola-Kirchhoff stress tensors $\overline{\mathbf{S}}_{\mathrm{vol},i}$ and $\widetilde{\mathbf{S}}_{\mathrm{dev},ij}$ and the elasticity tensors $\overline{\mathbb{D}}_{\mathrm{vol},i}$ and $\widetilde{\mathbb{D}}_{\mathrm{dev},ij}$. The elasticity tensors can then be rearranged into 3×3 matrices, denoted as $\overline{\mathbf{D}}_{\mathrm{vol},i}$ and $\widetilde{\mathbf{D}}_{\mathrm{dev},ij}$, by using Voigt notation.

In order to compute the force state, the first Piola-Kirchhoff stress tensor $\mathbf{P}$ is required. Since $\mathbf{P} = \mathbf{F}\,\mathbf{S}$, the first Piola-Kirchhoff stress tensor including the increment due to the increment $\Delta\mathbf{U}$ is given as

$$\mathbf{P} + \Delta\mathbf{P} = (\mathbf{F}+\Delta\mathbf{F})(\mathbf{S}+\Delta\mathbf{S}) = \mathbf{F}\,\mathbf{S} + \Delta\mathbf{F}\,\mathbf{S} + \mathbf{F}\,\Delta\mathbf{S} + \Delta\mathbf{F}\,\Delta\mathbf{S}\,, \tag{33}$$

Algorithm 1 Computation of the tangent stiffness matrix and the internal force vector.

```
Inizialize $\mathbf{K}$ and $\mathbf{f}_{\mathrm{int}}$ with all zero components
for each bond $\boldsymbol{\xi}_{ij}$ do
    Compute $\overline{\mathbf{K}}_i$ and $\widetilde{\mathbf{K}}_{ij}$ respectively from Eq. (17) and Eq. (21)
    Rearrange $\overline{\mathbf{K}}_i$ and $\widetilde{\mathbf{K}}_{ij}$ into $\overline{\mathbf{B}}_i$ and $\widetilde{\mathbf{B}}_{ij}$ with Eq. (31)
    Inizialize $\overline{\mathbf{N}}_i$ and $\widetilde{\mathbf{N}}_{ij}$ with all zero components
    for each node $k$ within $\mathcal{H}_i$ do
        $\overline{\mathbf{N}}_i(1:2,2i-1) = \overline{\mathbf{N}}_i(1:2,2i-1) - \underline{\omega}\langle\boldsymbol{\xi}_{ik}\rangle\,\xi_{ik}\,\beta_{ik}\Delta V$
        $\overline{\mathbf{N}}_i(1:2,2k-1) = \overline{\mathbf{N}}_i(1:2,2k-1) + \underline{\omega}\langle\boldsymbol{\xi}_{ik}\rangle\,\xi_{ik}\,\beta_{ik}\Delta V$
        $\overline{\mathbf{N}}_i(3:4,2i) = \overline{\mathbf{N}}_i(1:2,2i) - \underline{\omega}\langle\boldsymbol{\xi}_{ik}\rangle\,\xi_{ik}\,\beta_{ik}\Delta V$
        $\overline{\mathbf{N}}_i(3:4,2k) = \overline{\mathbf{N}}_i(3:4,2k) + \underline{\omega}\langle\boldsymbol{\xi}_{ik}\rangle\,\xi_{ik}\,\beta_{ik}\Delta V$
    end for
    for each node $k$ within $\mathcal{H}_i \cap \mathcal{H}_j$ do
        $\widetilde{\mathbf{N}}_{ij}(1:2,2i-1) = \widetilde{\mathbf{N}}_{ij}(1:2,2i-1) - \underline{\omega}\langle\boldsymbol{\xi}_{ik}\rangle\,\xi_{ik}\,\beta_{ik}\Delta V$
        $\widetilde{\mathbf{N}}_{ij}(1:2,2k-1) = \widetilde{\mathbf{N}}_{ij}(1:2,2k-1) + \underline{\omega}\langle\boldsymbol{\xi}_{ik}\rangle\,\xi_{ik}\,\beta_{ik}\Delta V$
        $\widetilde{\mathbf{N}}_{ij}(3:4,2i) = \widetilde{\mathbf{N}}_{ij}(3:4,2i) - \underline{\omega}\langle\boldsymbol{\xi}_{ik}\rangle\,\xi_{ik}\,\beta_{ik}\Delta V$
        $\widetilde{\mathbf{N}}_{ij}(3:4,2k) = \widetilde{\mathbf{N}}_{ij}(3:4,2k) + \underline{\omega}\langle\boldsymbol{\xi}_{ik}\rangle\,\xi_{ik}\,\beta_{ik}\Delta V$
    end for
    $\overline{\mathbf{F}}_i = \overline{\mathbf{B}}_i\,\overline{\mathbf{N}}_i\,\mathbf{U} + \mathbf{I}$
    $\widetilde{\mathbf{F}}_{ij} = \widetilde{\mathbf{B}}_{ij}\,\widetilde{\mathbf{N}}_{ij}\,\mathbf{U} + \mathbf{I}$
    Compute $\overline{\mathbf{S}}_{\mathrm{vol},i}$ and $\overline{\mathbf{D}}_{\mathrm{vol},i}$ with $\overline{\mathbf{F}}_{\mathrm{vol},i} = \overline{J}^{\frac{1}{3}}\mathbf{I}$ using, for example, Eq. (3)
    Compute $\widetilde{\mathbf{S}}_{\mathrm{dev},ij}$ and $\widetilde{\mathbf{D}}_{\mathrm{dev},ij}$ with $\widetilde{\mathbf{F}}_{\mathrm{dev},ij} = \widetilde{J}^{-\frac{1}{3}}\widetilde{\mathbf{F}}_{ij}$ using, for example, Eq. (4)
    Rearrange $\overline{\mathbf{S}}_{\mathrm{vol},i}$ and $\widetilde{\mathbf{S}}_{\mathrm{dev},ij}$ into $\overline{\mathbf{L}}_{\mathrm{vol},i}$ and $\widetilde{\mathbf{L}}_{\mathrm{dev},ij}$ with Eq. (36)
    Rearrange $\overline{\mathbf{F}}_i$ and $\widetilde{\mathbf{F}}_{ij}$ into $\overline{\mathbf{G}}_i$ and $\widetilde{\mathbf{G}}_{ij}$ with Eq. (39)
    Compute $\overline{\mathbf{Q}}_{ij}$ and $\widetilde{\mathbf{Q}}_{ij}$ from Eq. (42)
    $\underline{\hat{\mathbf{T}}}\langle\boldsymbol{\xi}_{ij}\rangle = \underline{\omega}\langle\boldsymbol{\xi}_{ij}\rangle\left[\overline{\mathbf{Q}}_{ij}\,\overline{\mathbf{F}}_i\,\overline{\mathbf{S}}_{\mathrm{vol},i} + \frac{N_{ij}}{N_i}\,\widetilde{\mathbf{Q}}_{ij}\,\widetilde{\mathbf{F}}_{ij}\,\widetilde{\mathbf{S}}_{\mathrm{dev},ij}\right]$
    $\mathbf{f}_{\mathrm{int}}(2i-1:2i) = \mathbf{f}_{\mathrm{int}}(2i-1:2i,:) - \underline{\hat{\mathbf{T}}}\langle\boldsymbol{\xi}_{ij}\rangle\,\beta_{ij}\Delta V^2$
    $\mathbf{f}_{\mathrm{int}}(2j-1:2j) = \mathbf{f}_{\mathrm{int}}(2j-1:2j,:) + \underline{\hat{\mathbf{T}}}\langle\boldsymbol{\xi}_{ij}\rangle\,\beta_{ij}\Delta V^2$
    $\mathbf{K}_{\Delta\underline{\hat{\mathbf{T}}}} = \underline{\omega}\langle\boldsymbol{\xi}_{ij}\rangle\left[\overline{\mathbf{Q}}_{ij}\left(\overline{\mathbf{L}}_{\mathrm{vol},i} + \overline{\mathbf{G}}_i^{\top}\,\overline{\mathbf{D}}_{\mathrm{vol},i}\,\overline{\mathbf{G}}_i\right)\overline{\mathbf{B}}_i\,\overline{\mathbf{N}}_i + \frac{N_{ij}}{N_i}\,\widetilde{\mathbf{Q}}_{ij}\left(\widetilde{\mathbf{L}}_{\mathrm{dev},ij} + \widetilde{\mathbf{G}}_{ij}^{\top}\,\widetilde{\mathbf{D}}_{\mathrm{dev},ij}\,\widetilde{\mathbf{G}}_{ij}\right)\widetilde{\mathbf{B}}_{ij}\,\widetilde{\mathbf{N}}_{ij}\right]$
    $\mathbf{K}(2i-1:2i,:) = \mathbf{K}(2i-1:2i,:) - \mathbf{K}_{\Delta\underline{\hat{\mathbf{T}}}}\,\beta_{ij}\Delta V^2$
    $\mathbf{K}(2j-1:2j,:) = \mathbf{K}(2j-1:2j,:) + \mathbf{K}_{\Delta\underline{\hat{\mathbf{T}}}}\,\beta_{ij}\Delta V^2$
end for
Return $\mathbf{K}$, $\mathbf{f}_{\mathrm{int}}$
```

where $\Delta\mathbf{P}$, $\Delta\mathbf{S}$, and $\Delta\mathbf{F}$ are the first and second Piola-Kirchhoff stress tensors and the deformation gradient tensor due to the increment $\Delta\mathbf{U}$, respectively. Since Newton-Raphson procedures work with linearized equations, the term $\Delta\mathbf{F}\,\Delta\mathbf{S}$ of Eq. (33) is neglected. The term $\mathbf{P} = \mathbf{F}\,\mathbf{S}$ is used to compute the contribution of bond $\boldsymbol{\xi}_{ij}$ to the internal force vector, whereas the term $\Delta\mathbf{P} = \Delta\mathbf{F}\,\mathbf{S} + \mathbf{F}\,\Delta\mathbf{S}$ is used to compute the contribution of bond $\boldsymbol{\xi}_{ij}$ in the tangent stiffness matrix. The volumetric and deviatoric parts of the former term are computed as

$$\overline{\mathbf{P}}_{\mathrm{vol},i} = \overline{\mathbf{F}}_i\,\overline{\mathbf{S}}_{\mathrm{vol},i}\,, \qquad \widetilde{\mathbf{P}}_{\mathrm{dev},ij} = \widetilde{\mathbf{F}}_{ij}\,\widetilde{\mathbf{S}}_{\mathrm{dev},ij}\,, \tag{34}$$

whereas those of the latter term as

$$\Delta\overline{\mathbf{P}}_{\mathrm{vol},i} = \Delta\overline{\mathbf{F}}_i\,\overline{\mathbf{S}}_{\mathrm{vol},i} + \overline{\mathbf{F}}_i\,\Delta\overline{\mathbf{S}}_{\mathrm{vol},i}\,, \qquad \Delta\widetilde{\mathbf{P}}_{\mathrm{dev},ij} = \Delta\widetilde{\mathbf{F}}_{ij}\,\widetilde{\mathbf{S}}_{\mathrm{dev},ij} + \widetilde{\mathbf{F}}_{ij}\,\Delta\widetilde{\mathbf{S}}_{\mathrm{dev},ij}\,. \tag{35}$$

The computation of the terms in Eq. (35) is shown hereinafter.

To compute the first terms of $\Delta\mathbf{P}$ in the form $\Delta\mathbf{F}\,\mathbf{S}$, we rearrange the second Piola-Kirchhoff stress tensor into

$$\overline{\mathbf{L}}_{\mathrm{vol},i} = \begin{bmatrix} \overline{\mathbf{S}}_{\mathrm{vol},i} & \mathbf{0} \\ \mathbf{0} & \overline{\mathbf{S}}_{\mathrm{vol},i} \end{bmatrix}, \qquad \widetilde{\mathbf{L}}_{\mathrm{dev},ij} = \begin{bmatrix} \widetilde{\mathbf{S}}_{\mathrm{dev},ij} & \mathbf{0} \\ \mathbf{0} & \widetilde{\mathbf{S}}_{\mathrm{dev},ij} \end{bmatrix}, \tag{36}$$

where $\overline{\mathbf{L}}_{\mathrm{vol},i}$ and $\widetilde{\mathbf{L}}_{\mathrm{dev},ij}$ are 4×4 matrices. Therefore, the first term to determine $\Delta\overline{\mathbf{P}}_i$ and $\Delta\widetilde{\mathbf{P}}_{ij}$ are respectively computed as

$$\overline{\mathbf{L}}_{\mathrm{vol},i}\,\Delta\overline{\mathbf{F}}_i = \overline{\mathbf{L}}_{\mathrm{vol},i}\,\overline{\mathbf{B}}_i\,\overline{\mathbf{N}}_i\,\Delta\mathbf{U}\,, \qquad \widetilde{\mathbf{L}}_{\mathrm{dev},ij}\,\Delta\widetilde{\mathbf{F}}_{ij} = \widetilde{\mathbf{L}}_{\mathrm{dev},ij}\,\widetilde{\mathbf{B}}_{ij}\,\widetilde{\mathbf{N}}_{ij}\,\Delta\mathbf{U}\,. \tag{37}$$

The increment of the second Piola-Kirchhoff stress tensor can be expressed as $\Delta\mathbf{S} = \mathbb{D} : (\Delta\mathbf{e} + \Delta\boldsymbol{\eta})$, where $\mathbf{e}$ and $\boldsymbol{\eta}$ are the linear and non-linear parts of the Green-Lagrange strain tensor, respectively (see, for example, [51, section 3.4]). The non-linear part can be neglected because of the linearization used within the Newton-Raphson method. On the other hand, the linear part of the Green-Lagrange strain tensor can be computed (in vector form) as

$$\Delta\bar{\mathbf{e}}_i = \begin{bmatrix} \Delta\bar{\mathbf{e}}_i(1,1) \\ \Delta\bar{\mathbf{e}}_i(2,2) \\ 2\Delta\bar{\mathbf{e}}_i(1,2) \end{bmatrix} = \bar{\mathbf{G}}_i\,\Delta\bar{\mathbf{F}}_i\,, \qquad \Delta\tilde{\mathbf{e}}_{ij} = \begin{bmatrix} \Delta\tilde{\mathbf{e}}_{ij}(1,1) \\ \Delta\tilde{\mathbf{e}}_{ij}(2,2) \\ 2\Delta\tilde{\mathbf{e}}_{ij}(1,2) \end{bmatrix} = \tilde{\mathbf{G}}_{ij}\,\Delta\tilde{\mathbf{F}}_{ij}\,, \tag{38}$$

where $\bar{\mathbf{G}}_i$ and $\tilde{\mathbf{G}}_{ij}$ are 3×4 matrices assembled as

$$\bar{\mathbf{G}}_i = \begin{bmatrix} \bar{\mathbf{F}}_i(1,1) & 0 & \bar{\mathbf{F}}_i(2,1) & 0 \\ 0 & \bar{\mathbf{F}}_i(1,2) & 0 & \bar{\mathbf{F}}_i(2,2) \\ \bar{\mathbf{F}}_i(1,2) & \bar{\mathbf{F}}_i(1,1) & \bar{\mathbf{F}}_i(2,2) & \bar{\mathbf{F}}_i(2,1) \end{bmatrix}, \qquad \tilde{\mathbf{G}}_{ij} = \begin{bmatrix} \tilde{\mathbf{F}}_{ij}(1,1) & 0 & \tilde{\mathbf{F}}_{ij}(2,1) & 0 \\ 0 & \tilde{\mathbf{F}}_{ij}(1,2) & 0 & \tilde{\mathbf{F}}_{ij}(2,2) \\ \tilde{\mathbf{F}}_{ij}(1,2) & \tilde{\mathbf{F}}_{ij}(1,1) & \tilde{\mathbf{F}}_{ij}(2,2) & \tilde{\mathbf{F}}_{ij}(2,1) \end{bmatrix}. \tag{39}$$

The transpose of these matrices can be also used to compute the second terms of $\Delta\bar{\mathbf{P}}$ in the form $\mathbf{F}\,\Delta\mathbf{S}$, namely

$$\bar{\mathbf{G}}_i^{\top} \begin{bmatrix} \Delta\bar{\mathbf{S}}_{\mathrm{vol},i}(1,1) \\ \Delta\bar{\mathbf{S}}_{\mathrm{vol},i}(2,2) \\ \Delta\bar{\mathbf{S}}_{\mathrm{vol},i}(1,2) \end{bmatrix} = \bar{\mathbf{G}}_i^{\top}\,\bar{\mathbf{D}}_{\mathrm{vol},i}\,\Delta\bar{\mathbf{e}}_i\,, \qquad \tilde{\mathbf{G}}_{ij}^{\top} \begin{bmatrix} \Delta\tilde{\mathbf{S}}_{\mathrm{dev},ij}(1,1) \\ \Delta\tilde{\mathbf{S}}_{\mathrm{dev},ij}(2,2) \\ \Delta\tilde{\mathbf{S}}_{\mathrm{dev},ij}(1,2) \end{bmatrix} = \tilde{\mathbf{G}}_{ij}^{\top}\,\tilde{\mathbf{D}}_{\mathrm{dev},ij}\,\Delta\tilde{\mathbf{e}}_{ij}\,, \tag{40}$$

where the increments of the linear parts of the strain tensors (see Eq. 38): $\Delta\bar{\mathbf{e}}_i = \bar{\mathbf{G}}_i\,\bar{\mathbf{B}}_i\,\bar{\mathbf{N}}_i\,\Delta\mathbf{U}$ and $\Delta\tilde{\mathbf{e}}_{ij} = \tilde{\mathbf{G}}_{ij}\,\tilde{\mathbf{B}}_{ij}\,\tilde{\mathbf{N}}_{ij}\,\Delta\mathbf{U}$. Finally, the increments of the first Piola-Kirchhoff stress tensor (in vector form) are given as

$$\Delta\bar{\mathbf{P}}_{\mathrm{vol},i} = \begin{bmatrix} \Delta\bar{\mathbf{P}}_{\mathrm{vol},i}(1,1) \\ \Delta\bar{\mathbf{P}}_{\mathrm{vol},i}(1,2) \\ \Delta\bar{\mathbf{P}}_{\mathrm{vol},i}(2,1) \\ \Delta\bar{\mathbf{P}}_{\mathrm{vol},i}(2,2) \end{bmatrix} = \left(\bar{\mathbf{L}}_{\mathrm{vol},i} + \bar{\mathbf{G}}_i^{\top}\,\bar{\mathbf{D}}_{\mathrm{vol},i}\,\bar{\mathbf{G}}_i\right)\bar{\mathbf{B}}_i\,\bar{\mathbf{N}}_i\,\Delta\mathbf{U}\,,$$

$$\Delta\tilde{\mathbf{P}}_{\mathrm{dev},ij} = \begin{bmatrix} \Delta\tilde{\mathbf{P}}_{\mathrm{dev},ij}(1,1) \\ \Delta\tilde{\mathbf{P}}_{\mathrm{dev},ij}(1,2) \\ \Delta\tilde{\mathbf{P}}_{\mathrm{dev},ij}(2,1) \\ \Delta\tilde{\mathbf{P}}_{\mathrm{dev},ij}(2,2) \end{bmatrix} = \left(\tilde{\mathbf{L}}_{\mathrm{dev},ij} + \tilde{\mathbf{G}}_{ij}^{\top}\,\tilde{\mathbf{D}}_{\mathrm{dev},ij}\,\tilde{\mathbf{G}}_{ij}\right)\tilde{\mathbf{B}}_{ij}\,\tilde{\mathbf{N}}_{ij}\,\Delta\mathbf{U}\,. \tag{41}$$

To finally compute the force state for each bond, we assemble the following 2×4 matrices:

$$\bar{\mathbf{Q}}_{ij} = \begin{bmatrix} \bar{\mathbf{q}}_{ij}^{\top} & \mathbf{0} \\ \mathbf{0} & \bar{\mathbf{q}}_{ij}^{\top} \end{bmatrix}, \qquad \tilde{\mathbf{Q}}_{ij} = \begin{bmatrix} \tilde{\mathbf{q}}_{ij}^{\top} & \mathbf{0} \\ \mathbf{0} & \tilde{\mathbf{q}}_{ij}^{\top} \end{bmatrix}, \tag{42}$$

where $\bar{\mathbf{q}}_{ij} = \left(\bar{\mathbf{K}}_i\right)^{-1}\boldsymbol{\xi}_{ij}$ and $\tilde{\mathbf{q}}_{ij} = \left(\tilde{\mathbf{K}}_{ij}\right)^{-1}\boldsymbol{\xi}_{ij}$ are 1×2 vectors. The force state and its increment are computed from the previous formulae, respectively, as

$$\hat{\underline{\mathbf{T}}}\langle\boldsymbol{\xi}_{ij}\rangle = \underline{\omega}\langle\boldsymbol{\xi}_{ij}\rangle\left[\bar{\mathbf{Q}}_{ij}\,\bar{\mathbf{F}}_i\,\bar{\mathbf{S}}_{\mathrm{vol},i} + \frac{N_{ij}}{N_i}\,\tilde{\mathbf{Q}}_{ij}\,\tilde{\mathbf{F}}_{ij}\,\tilde{\mathbf{S}}_{\mathrm{dev},ij}\right], \tag{43}$$

$$\Delta\hat{\underline{\mathbf{T}}}\langle\boldsymbol{\xi}_{ij}\rangle = \underline{\omega}\langle\boldsymbol{\xi}_{ij}\rangle\left[\bar{\mathbf{Q}}_{ij}\left(\bar{\mathbf{L}}_{\mathrm{vol},i} + \bar{\mathbf{G}}_i^{\top}\,\bar{\mathbf{D}}_{\mathrm{vol},i}\,\bar{\mathbf{G}}_i\right)\bar{\mathbf{B}}_i\,\bar{\mathbf{N}}_i + \frac{N_{ij}}{N_i}\,\tilde{\mathbf{Q}}_{ij}\left(\tilde{\mathbf{L}}_{\mathrm{dev},ij} + \tilde{\mathbf{G}}_{ij}^{\top}\,\tilde{\mathbf{D}}_{\mathrm{dev},ij}\,\tilde{\mathbf{G}}_{ij}\right)\tilde{\mathbf{B}}_{ij}\,\tilde{\mathbf{N}}_{ij}\right]\Delta\mathbf{U}\,, \tag{44}$$

As mentioned previously, the force state equation is used to assemble the internal force vector $\mathbf{f}_{\mathrm{int}}$, whereas the equation of its increment is used to assemble the tangent stiffness matrix $\mathbf{K}$, as shown in Algorithm 1 (lines 25–30). In this algorithm, the force state $-\left(\hat{\underline{\mathbf{T}}}\langle\boldsymbol{\xi}_{ij}\rangle + \Delta\hat{\underline{\mathbf{T}}}\langle\boldsymbol{\xi}_{ij}\rangle\right)$ is applied to node i and $\left(\hat{\underline{\mathbf{T}}}\langle\boldsymbol{\xi}_{ij}\rangle + \Delta\hat{\underline{\mathbf{T}}}\langle\boldsymbol{\xi}_{ij}\rangle\right)$ to node j. Therefore, the term $\left(\hat{\underline{\mathbf{T}}}\langle\boldsymbol{\xi}_{ji}\rangle + \Delta\hat{\underline{\mathbf{T}}}\langle\boldsymbol{\xi}_{ji}\rangle\right)$ of the summation of Eq. (29) is applied to node i when the bond $\boldsymbol{\xi}_{ij}$ is considered in the for loop.

4. Illustrative examples and benchmark problems

This section presents several illustrative examples and benchmark problems involving both homogeneous and inhomogeneous finite deformations in isotropic hyperelastic solids, aimed at validating the performance of the proposed correspondence with selective bond-associated deformation gradient.

4.1. Homogeneous deformations

Two homogeneous deformation problems are first analyzed. A Neo-Hookean nearly incompressible strain energy function is assumed, considering two illustrative values of the initial bulk modulus to initial shear modulus ratio, κ/μ, corresponding to equivalent Poisson's ratios of $\nu = 0.475$ ($\kappa/\mu = 2\times10^1$) and $\nu = 0.49995$ ($\kappa/\mu = 1\times10^4$), respectively. The first case represents a reference value commonly adopted as a default in commercial finite element software and lies well below the typical range characterizing filled elastomers (κ/μ ranging from 5×10^1 to 2×10^2) [49]. The second value is typically employed to approximate the condition of near

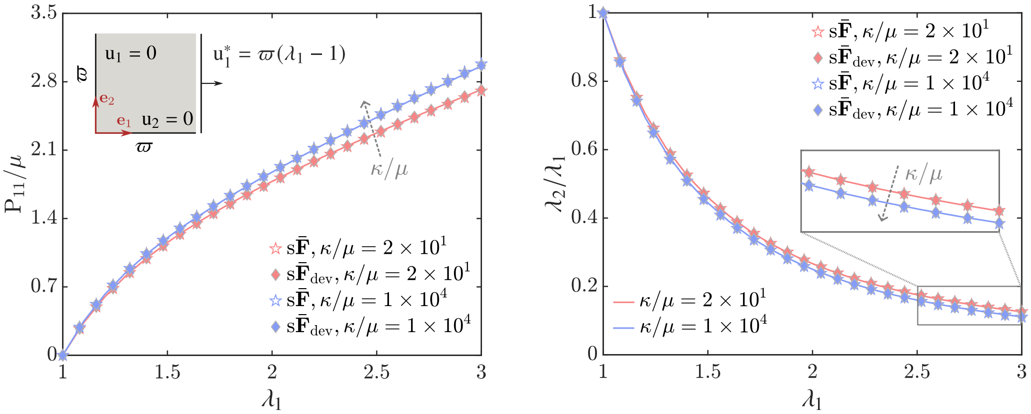

Fig. 3. Neo-Hookean solid under homogeneous deformation (simple tension) considering different κ/μ ratios: P_{11} first Piola-Kirchhoff stress (left) and λ_2/λ_1 stretch ratio (right) as a function of λ_1 stretch, obtained by correspondence model with bond-associated deformation gradient $\widetilde{\mathbf{F}}$ (s$\bar{\mathbf{F}}$ in the legend stands for "method with stabilization of the deformation gradient tensor") and selective bond-associated deformation gradient $\widehat{\mathbf{F}}$ (s$\bar{\mathbf{F}}_{\text{dev}}$ in the legend stands for "method with stabilization of the deviatoric deformation gradient tensor"). Solid lines denote the reference hyperelastic continuum solutions.

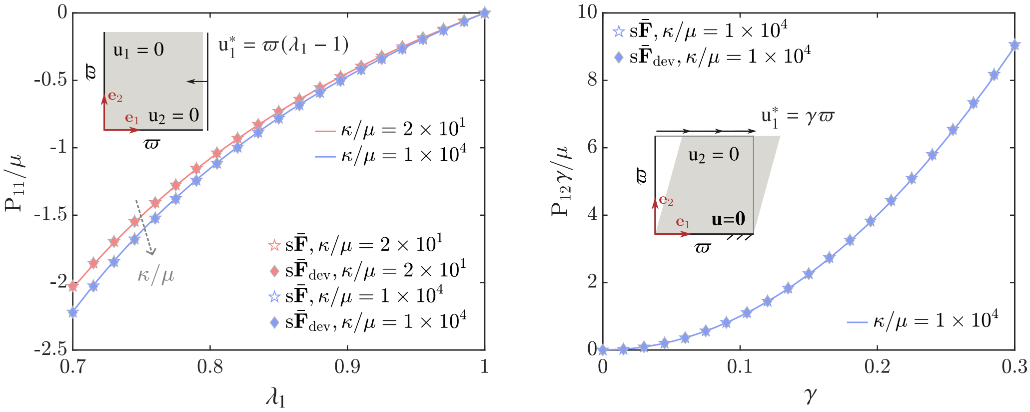

Fig. 4. Neo-Hookean solid under homogeneous deformation: P_{11} first Piola-Kirchhoff stress corresponding to different κ/μ ratios in simple compression (left) and P_{12} first Piola-Kirchhoff stress in simple shear (right), obtained by correspondence model with bond-associated deformation gradient $\widetilde{\mathbf{F}}$ (s$\bar{\mathbf{F}}$ in the legend stands for "method with stabilization of the deformation gradient tensor") and selective bond-associated deformation gradient $\widehat{\mathbf{F}}$ (s$\bar{\mathbf{F}}_{\text{dev}}$ in the legend stands for "method with stabilization of the deviatoric deformation gradient tensor"). Solid lines denote the reference hyperelastic continuum solutions.

incompressibility in rubber-like materials and soft tissues and can be considered a practical upper bound for unfilled elastomers, for which κ/μ typically ranges from 1×10^2 to 1×10^4. In particular, the two configurations characterized by affine displacement fields are defined over a regular square domain of side length ϖ. Given the orthonormal reference basis of unit vectors $\mathbf{e}_1$ and $\mathbf{e}_2$, a uniform extension (compression) with lateral contraction (expansion), and a simple shear deformation state are considered, respectively (Figs. 3 and 4). In the first case, corresponding to plane strain deformation, the associated deformation gradient tensor reads

$$\mathbf{F} = \lambda_1 \mathbf{e}_1 \otimes \mathbf{e}_1 + \lambda_2 \mathbf{e}_2 \otimes \mathbf{e}_2 + \mathbf{e}_3 \otimes \mathbf{e}_3 \tag{45}$$

where λ_1 is the principal stretch in the direction of extension (compression) and $\lambda_2 = J/\lambda_1$, the corresponding state of stress being referred to as simple tension when $\lambda_1 > 1$ and simple compression if $\lambda_1 < 1$ [69]. The second homogeneous state is that of an isochoric plane deformation for which there exists a set of line elements whose orientation is such that they are unchanged in length and direction by the deformation. Let $\mathbf{e}_1$ define this orientation.The associated gradient deformation tensor in this case reads

$$\mathbf{F} = \mathbf{I} + \gamma \mathbf{e}_1 \otimes \mathbf{e}_2 \tag{46}$$

where γ is denoted as the amount of shear. It is observed that the solutions obtained using both the bond-associated correspondence model and the newly proposed selective correspondence model yield highly accurate and mutually consistent results when compared to the standard finite elasticity solution. In particular, both correspondence models are capable of accurately reproducing the stress

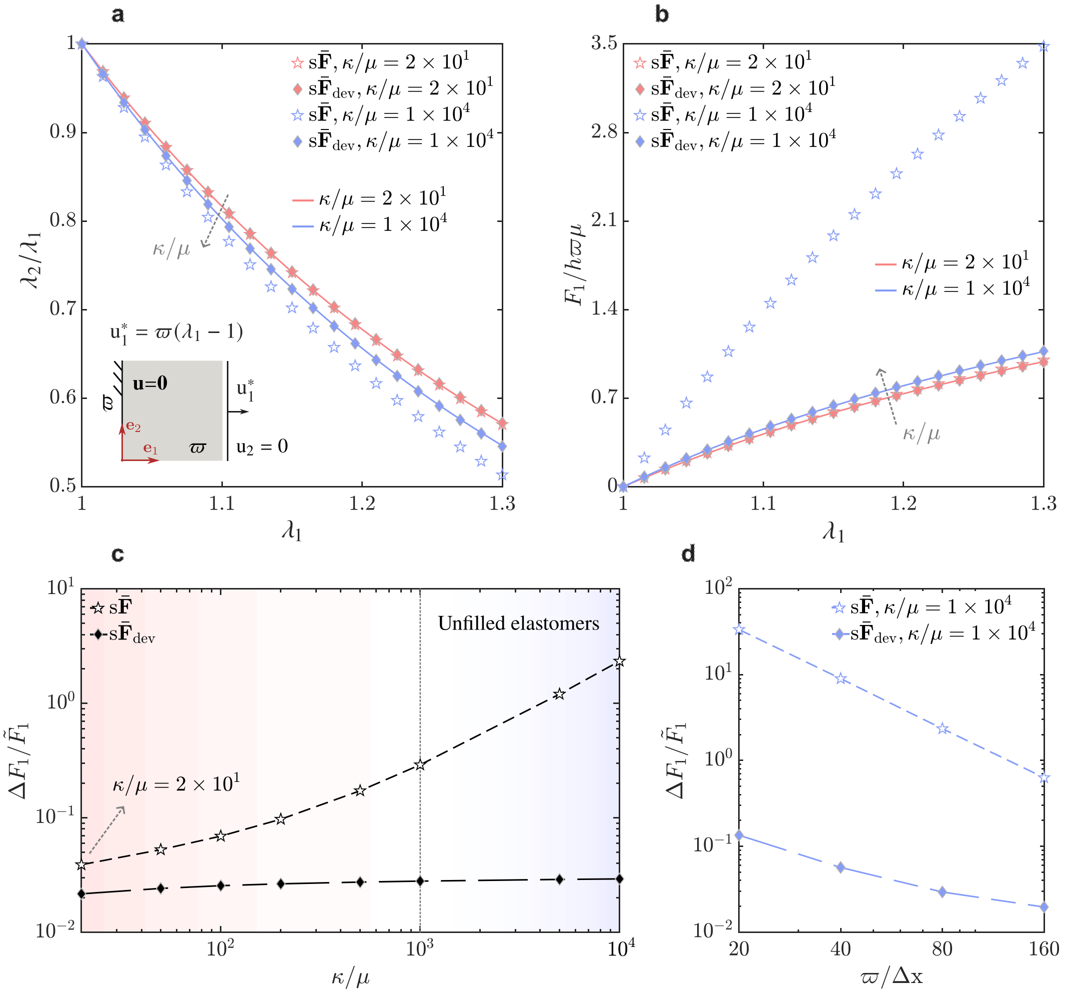

Fig. 5. Neo-Hookean solid under inhomogeneous extension: Boundary conditions of the problem and maximum λ_2/λ_1 stretch ratio as a function of the imposed λ_1 stretch, corresponding to different κ/μ. Elastic solution obtained correspondence model ($\varpi/\Delta x = 80$) with bond-associated deformation gradient $\widetilde{\mathbf{F}}$ ($\text{s}\bar{\mathbf{F}}$ in the legend stands for "method with stabilization of the deformation gradient tensor") and selective bond-associated deformation gradient $\widehat{\mathbf{F}}$ ($\text{s}\bar{\mathbf{F}}_{\text{dev}}$ in the legend stands for "method with stabilization of the deviatoric deformation gradient tensor") (**a**); Normalized axial reaction force F_1 as function of the imposed axial stretch (**b**); Normalized relative difference of the computed axial force reaction $\Delta F_1/\tilde{F}_1$ (with $\tilde{F}_1$ being the reference value of the hyperelastic continuum) as function of the κ/μ ratio (**c**); Normalized relative difference of the computed axial force reaction $\Delta F_1/\tilde{F}_1$ corresponding to different grid spacings Δx of the regular square grid (**d**).

and displacement fields of the hyperelastic solid as predicted by classical continuum mechanics, for both moderate and nearly incompressible material behavior ($\kappa/\mu = 1 \times 10^1$ and $\kappa/\mu = 1 \times 10^4$, respectively)[1] Given the resulting affine displacement field, the numerical results are almost independent of the discretization used, as the non-local effects related to the horizon size are negligible. Under these conditions, the two correspondence schemes are therefore directly comparable and yield consistent predictions.

4.2. Inhomogeneous deformations

Focusing on the uniaxial case-which, among standard plane strain deformation modes, is of particular physical significance in revealing the compressibility effects of hyperelastic material response-a non-affine displacement field is considered. More specifically, a uniaxial tensile test under non-homogeneous deformation is examined. A square specimen of side length ϖ is modeled, clamped on one edge and stretched on the opposite edge, with the transverse displacement constrained (Fig. 5**a**). A Neo-Hookean strain energy function is adopted, characterized by an initial shear modulus μ, while different compressibility ratios κ/μ are considered within the range defined by the two representative extreme values previously introduced. It is observed that, in the case of moderate compressibility (lower bound, $\kappa/\mu = 2 \times 10^1$), both correspondence models are able to accurately reproduce the mechanical response

---

[1] In the case of simple shear, due to the inherently isochoric nature of the deformation state, a representative value of κ/μ is considered.

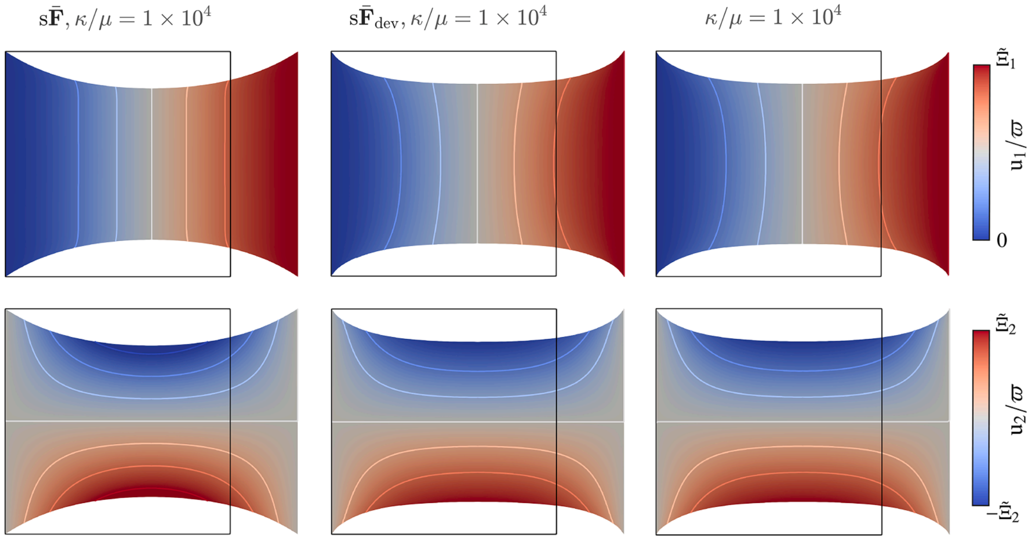

Fig. 6. Neo-Hookean solid under inhomogeneous extension: Nondimensional displacement fields and deformed configuration obtained by correspondence model with bond-associated deformation gradient $\widetilde{\mathbf{F}}$ (first column, $\mathrm{s}\bar{\mathbf{F}}$ in the legend stands for "method with stabilization of the deformation gradient tensor") and selective bond-associated deformation gradient $\widehat{\mathbf{F}}$ (second column, $\mathrm{s}\bar{\mathbf{F}}_{\mathrm{dev}}$ in the legend stands for "method with stabilization of the deviatoric deformation gradient tensor")in the case of $\kappa/\mu = 1 \times 10^4$. The reference solution corresponding to the classical hyperelastic continuum is reported in the third column. The limits of the colorbars are $\tilde{\Xi}_1 = 3/10$ and $\tilde{\Xi}_2 = 29/200$, respectively.

of the material, both in terms of kinematics and in terms of the overall stiffness of the system (Fig. 5**b**). However, this is not the case when the material exhibits strongly incompressible behavior. In particular, for $\kappa/\mu = 1 \times 10^4$-representing the upper bound of the considered range and corresponding to an almost incompressible response-only the correspondence model based on the selective bond-associated deformation gradient $\widehat{\mathbf{F}}$ is able to correctly reproduce the deformation state and the elastic energy stored in the deformed system, as shown in Figs. 5**a** – **b** and 6. It is worth noting that the selective bond-associated deformation gradient exhibits a robust and stable behavior, essentially independent of the specific value of the nondimensional compressibility ratio. In contrast, the classical bond-associated scheme shows a level of accuracy in reproducing the mechanical response of the hyperelastic material that is strongly dependent on the material's compressibility (Fig. 5**c**). It can be highlighted that even at the lower end of the considered κ/μ range, the accuracy of the selective scheme-evaluated in terms of the normalized relative difference in the computed axial reaction force, $\Delta F_1/\tilde{F}1$, with $\tilde{F}1$ being the reference value from the hyperelastic continuum-is nearly twice that of the bond-associated correspondence scheme. However, the classical scheme shows noticeable limitations when applied to values of κ/μ representative of most elastomers[2]. In particular, for compressibility ratios typical of unfilled elastomers (and soft biological tissues in undrained conditions), the classical bond-associated correspondence model appears to suffer significantly from volumetrick locking and divergence, such that the relative errors in the computed global stiffness of the system exceed 30 % when compared to the reference Neo-Hookean solution in classical elasticity (numerically obtained via a hybrid finite element formulation [49]). It is also important to note that the selective bond-associated correspondence scheme exhibits a high degree of accuracy even for relatively coarse grid spacing, while showing a typical convergent behavior as the grid is refined and then the horizon size is reduced (Fig. 5**d**).

Consider now the *Cook's membrane problem* in finite elasticity [70]. It consists of a tapered panel of nearly incompressible hyperelastic material clamped on one side while a shearing load is applied on the opposite side, and constitutes a standard test for combined bending and shear response with moderate distortion (Fig. 7). The trapezoidal panel of thickness h measures $L = 44\varpi$ on the left-hand side and $16\ \varpi = 4L/11$ on the right-hand side, with ϖ being the in-plane unit reference length measure. The two sides are parallel and $48\ \varpi = 12L/11$ apart. The top right-hand corner is initially $16\ \varpi$ above the top left-hand corner. The panel is clamped on its left edge and loaded in shear with a unit force on its right edge. It is composed of nearly incompressible neoHookean material with parameters $\mu = 4F_2/5h\varpi$ and $\kappa/\mu = 1 \times 10^4$ to enable comparison with the results of Simo and Armero [61] and Brink and Stein [50]. Fig. 8 shows that the correspondence model with selective bond-associated deformation gradient is characterized by fast convergence to the classical hyperelastic solution for reducing horizons, and shows good accuracy and effectiveness, even in the case of relatively coarse regular grid spacing. Due to the nearly-incompressible behavior, the solution obtained with the bond-associated correspondence model is significantly affected by locking phenomena, regardless of the grid spacing adopted (Fig. 8). Interestingly, the behavior observed for reduced grid spacings appears similar to that proper of linear displacement quadrilateral finite elements (usually referred to as Q4 FE).

---

[2] We may regard $\kappa/\mu = 1 \times 10^2$ as an effective threshold beyond which the accuracy of the bond-associated correspondence model significantly deteriorates. While this finding specifically concerns elastic problems, it reflects a general trend observed in commercial finite element software, where one-field formulations-both linear and higher-order-are typically deemed unsuitable for values of κ/μ beyond this limit[49].

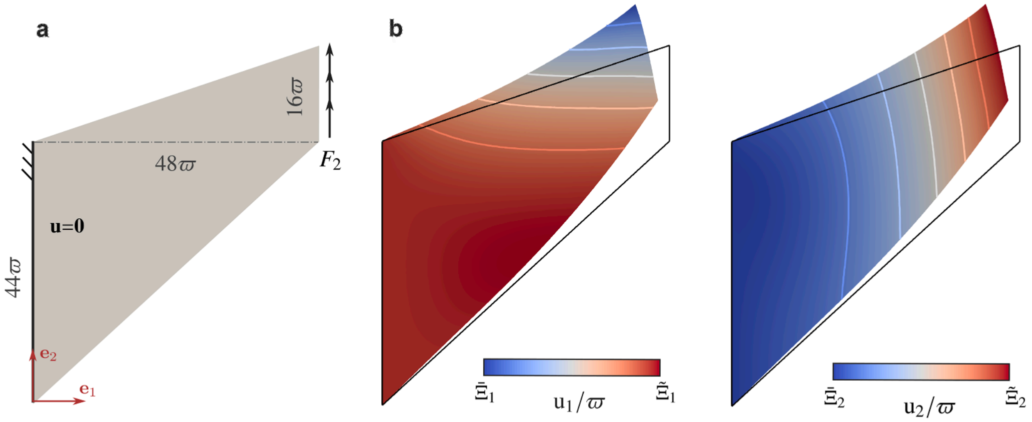

Fig. 7. Cook's membrane problem in finite elasticity under plane strain: Geometry and boundary conditions (**a**); Reference hyperelastic continuum solution (nondimensional displacement fields on deformed configuration) corresponding to a nearly-incompressible Neo-Hookean solid with $\mu = 4F_2/5h\varpi$ and $\kappa/\mu = 1 \times 10^4$. The limits of the colorbars are $\bar{\Xi}_1 = -29/5$ and $\tilde{\Xi}_1 = 31/100$ for u_1/ϖ, and $\bar{\Xi}_2 = -1/50$ and $\tilde{\Xi}_2 \approx 7$ for u_2/ϖ, respectively (**b**).

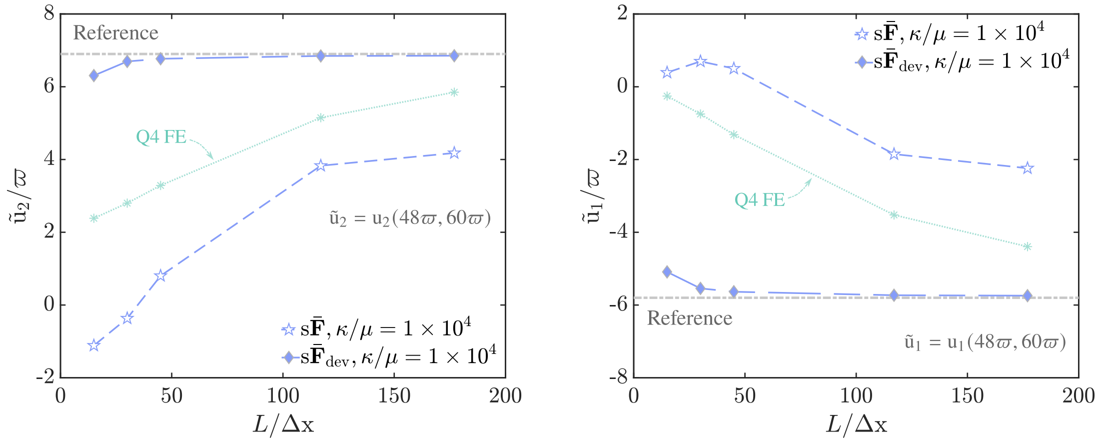

Fig. 8. Cook's membrane problem in finite elasticity under plane strain: Non-dimensional displacements of the reference point $\mathscr{P}(48\varpi, 60\varpi)$ obtained by correspondence model with bond-associated deformation gradient $\widetilde{\mathbf{F}}$ (s$\bar{\mathbf{F}}$ in the legend stands for "method with stabilization of the deformation gradient tensor") and selective bond-associated deformation gradient $\widehat{\mathbf{F}}$ (s$\bar{\mathbf{F}}_{\text{dev}}$ in the legend stands for "method with stabilization of the deviatoric deformation gradient tensor") considering different regular grid spacing Δx. Results corresponding to classical displacement linear quadrilateral (Q4) FE are also reported.

Moreover, the resulting deformed configuration clearly deviates from the reference solution of classical hyperelastyicity (Figs. 9 and 10), as the one-field formulation of (non-ordinary) state-based peridynamics with bond-associated deformation gradient seems not able to reproduce the bending deformation of the Neo-Hookean solid as well as its stored elastic energy.

A crack-tip problem is also considered in order to assess the performance of the proposed scheme in the presence of discontinuities and, therefore, highly non-homogeneous strain fields. In particular, we analyze a stationary crack in a two-dimensional geometry with slab width ϖ, length 4ϖ, and a crack of length ϖ, as detailed in Fig. 11. A similar setup in terms of layout and dimensions was considered by Buehler and Gao in their seminal work on local hyperelasticity at crack tips [71]. Starting from the undeformed configuration, a vertical displacement of magnitude $u_2^* = \varpi/8$ is imposed on both the upper and lower horizontal boundaries.

Due to the strong deformation inhomogeneity induced by the imposed loading, we also investigate the effect of different peridynamic influence function on the behavior of the correspondence model at fixed horizon size. To this end, the standard unit influence function $\underline{\bar{\omega}}\langle\xi\rangle = 1$ is considered alongside the usual influence function $\underline{\hat{\omega}}\langle\xi\rangle$ defined in Section 2.2. Focusing directly on the nearly incompressible case, the hyperelastic material considered for this nonlinear problem is a Neo-Hookean solid characterized by a bulk-to-shear modulus ratio $\kappa/\mu = 1 \times 10^4$. As shown in Fig. 11, locking phenomena lead to significant inconsistencies in the representation of the crack front and the crack opening displacement when using the bond-associated scheme. It is worth noting that, in this case, both influence functions produce altered crack front shapes. Specifically, the influence function $\hat{\omega}\langle\xi\rangle$ underestimates the maximum crack opening, while producing smoother crack edges; on the other hand, the unit influence function $\bar{\omega}\langle\xi\rangle$ overestimates the maximum opening and yields an almost linear crack edge profile over a large portion of the front. In contrast, the newly proposed correspon-

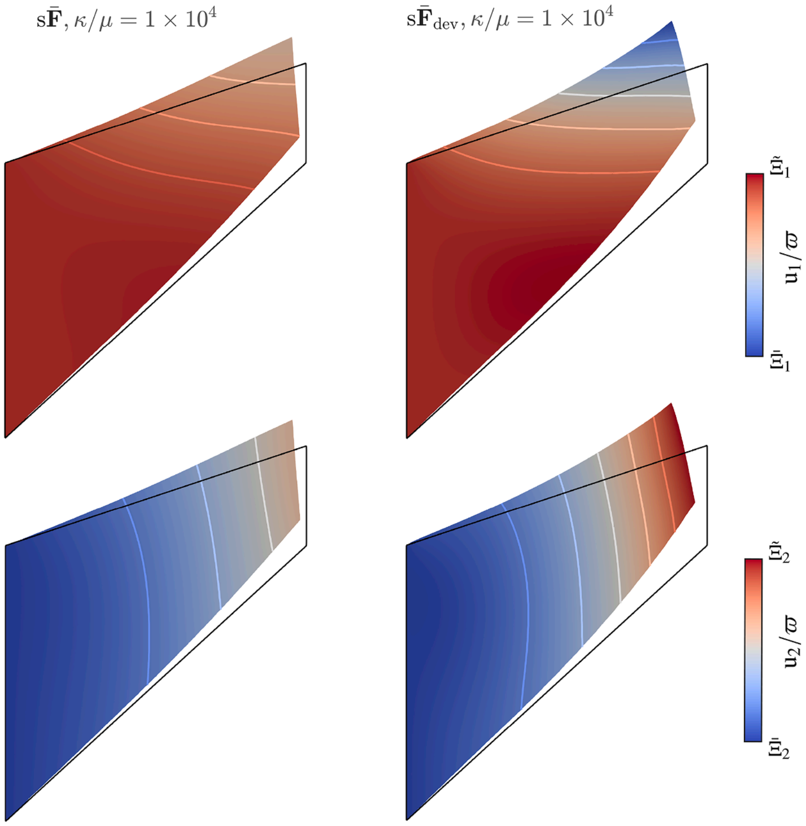

Fig. 9. Cook's membrane problem in finite elasticity under plane strain: Non-dimensional displacement fields and deformed configuration obtained by correspondence model with bond-associated deformation gradient $\widetilde{\mathbf{F}}$ (left, $\mathrm{s}\bar{\mathbf{F}}$ stands for "method with stabilization of the deformation gradient tensor") and selective bond-associated deformation gradient $\widehat{\mathbf{F}}$ (right, $\mathrm{s}\bar{\mathbf{F}}_{\mathrm{dev}}$ stands for "method with stabilization of the deviatoric deformation gradient tensor") considering $\Delta\mathrm{x} = L/120$. The limits of the colorbars are $\bar{\Xi}_1 = -29/5$ and $\tilde{\Xi}_1 = 31/100$ for u_1/ϖ, and $\bar{\Xi}_2 = -1/50$ and $\tilde{\Xi}_2 \approx 7$ for u_2/ϖ, respectively.

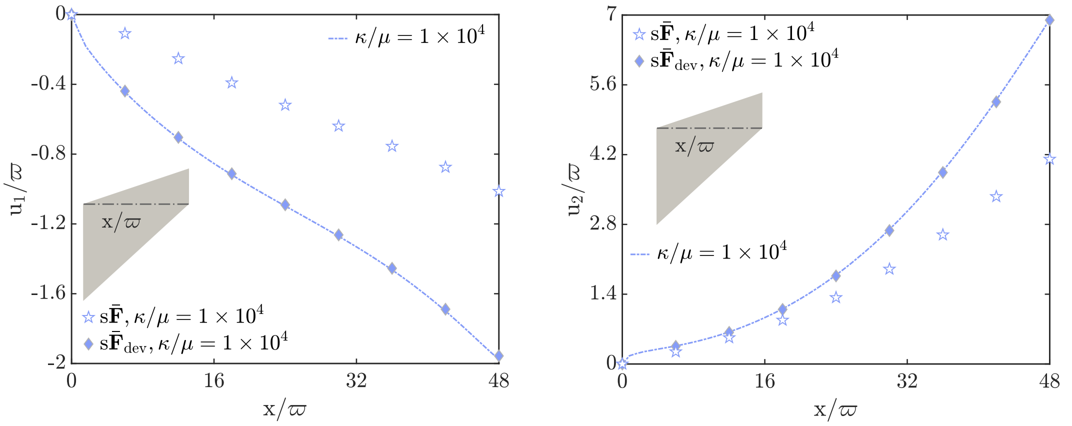

Fig. 10. Cook's membrane problem in finite elasticity under plane strain: Non-dimensional displacements along the abscissa $\mathrm{x}_2 = (L = 44\varpi)$ obtained by correspondence model with bond-associated deformation gradient $\widetilde{\mathbf{F}}$ ($\mathrm{s}\bar{\mathbf{F}}$ in the legend stands for "method with stabilization of the deformation gradient tensor") and selective bond-associated deformation gradient $\widehat{\mathbf{F}}$ ($\mathrm{s}\bar{\mathbf{F}}_{\mathrm{dev}}$ in the legend stands for "method with stabilization of the deviatoric deformation gradient tensor") considering $\Delta\mathrm{x} = L/120$. Dashed lines denote the reference classical continuum hyperelastic solution with $\kappa/\mu = 1 \times 10^4$.

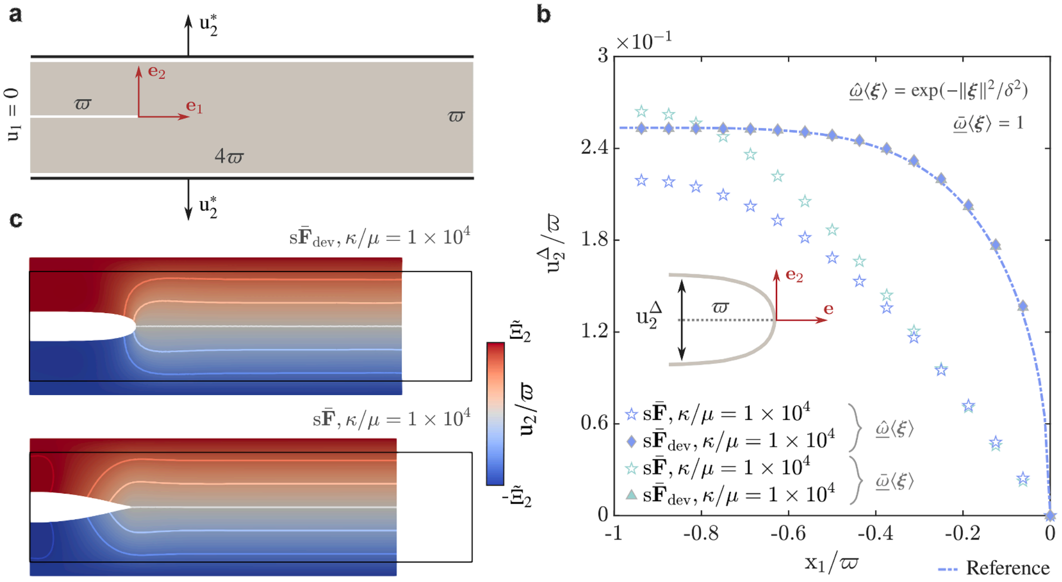

Fig. 11. Crack-tip problem in finite elasticity under plane strain: Geometry and boundary conditions (**a**); Crack opening displacement corresponding to $u_2 = \varpi/8$ and obtained by correspondence model with bond-associated deformation gradient $\widetilde{\mathbf{F}}$ (s$\bar{\mathbf{F}}$ in the legend stands for “method with stabilization of the deformation gradient tensor”) and selective bond-associated deformation gradient $\widehat{\mathbf{F}}$ (s$\bar{\mathbf{F}}_{\text{dev}}$ in the legend stands for “method with stabilization of the deviatoric deformation gradient tensor”) while assuming different influence functions (i.e. $\check{\underline{\omega}}\langle\xi\rangle$ and $\bar{\underline{\omega}}\langle\xi\rangle$) and $\Delta x = \varpi/120$. Dashed lines denote the reference classical continuum hyperelastic solution with $\kappa/\mu = 1 \times 10^4$ (**b**); Non-dimensional vertical displacement field and deformed configuration obtained using the bond-associated and the newly proposed selective schemes, assuming the unit influence function $\bar{\underline{\omega}}\langle\xi\rangle$. The colorbar limit is $\tilde{\Xi}_2 = 16/125$ (**c**).

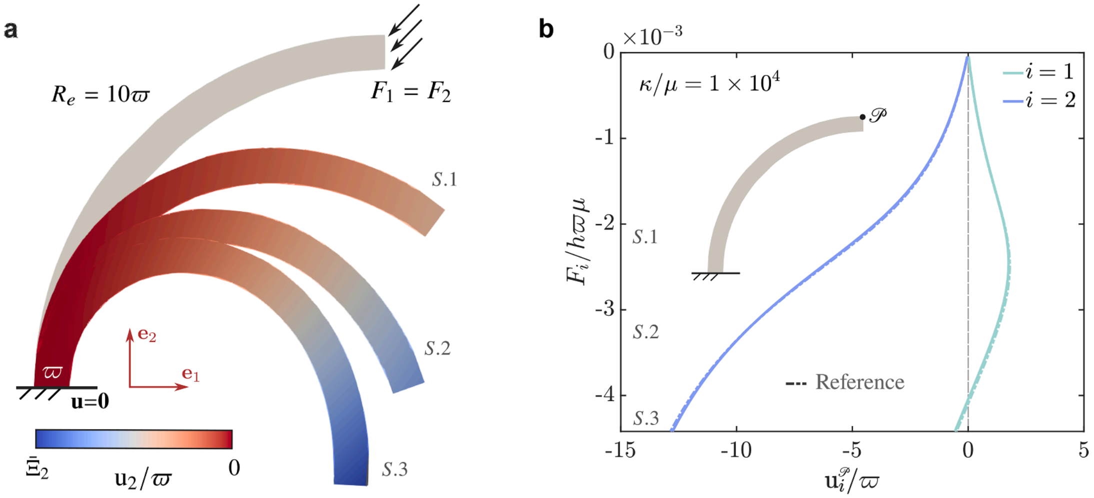

Fig. 12. Soft curved arch problem: Geometry, boundary conditions and deformed configurations obtained by correspondence model with selective bond-associated deformation gradient $\widehat{\mathbf{F}}$ (s$\bar{\mathbf{F}}_{\text{dev}}$ in the legend stands for “method with stabilization of the deviatoric deformation gradient tensor”) at three subsequent steps $S.i$ (**a**); Nondimensional applied force F_i-displacement $u_i^{\mathscr{P}}$ curve obtained adopting a regular grid spacing with $\Delta x = \varpi/20$. Dashed lines denote the reference solution corresponding to classical Neo-Hookean solid with $\mu/|F_1|h\varpi = 160$ and and $\kappa/\mu = 1 \times 10^4$. The colorbar limit is $\bar{\Xi}_2 = -32/25$ (**b**).

dence model based on the selective bond-associated deformation gradient accurately captures both the displacement field and the crack opening displacement, for arbitrary values of the abscissa x_1. In this case, the results are essentially independent of the specific influence function adopted.

Finally, a benchmark problem is considered to assess the performance of the proposed correspondence model in the presence of finite bending deformations and large displacements. Specifically, the cylindrical bending of a nearly-incompressible cantilever arch with thickness ϖ and external radius $R_e = 10\varpi$, subjected to an inclined compressive pressure, is analyzed. The compression load of magnitude F is applied at the tip-free end of the arc and inclined by an angle $\alpha_r = 5\pi/4$ with respect to the reference basis, with load component being $F_1 = F_2$. The detailed geometry and layout of the problem are reported in Fig. 12. Focusing on the nearly-incompressible case, the hyperelastic material is a Neo-Hookean solid with $\mu/|F_1|h\varpi = 160$ and $\kappa/\mu = 1 \times 10^4$. The discretization adopted considers a regular grid with spacing $\Delta x = \varpi/20$. Similar problems have been investigated in [72,73] within the framework of finite element formulations for finite elasticity. Solutions obtained by the present implementation of hyperelastic state-based model provide good results in accordance with the reference solution in classical continuum mechanics (obtained numerically adopting a hybrid linear FE formulation). The correspondence model based on the selective bond-associated deformation gradient also demonstrates, in the case of large displacements, a robust capability to accurately reproduce both the deformation field and the elastic energy stored in the hyperelastic solid. This holds true both qualitatively, in terms of the resulting deformed configuration, and quantitatively, in terms of the computed displacement field (Fig. 12).

These results clearly demonstrate that the proposed correspondence model is effective for finite elasticity with arbitrary compressibility and, in particular, is capable of accurately capturing the mechanical response of hyperelastic solids in the incompressible limit, while formally preserving the standard mathematical structure of discretized (non-ordinary) state-based-type peridynamic governing equations.

5. Conclusions

In this work, a correspondence model for peridynamic states has been presented in the framework of nearly incompressible finite elasticity. The approach is based on an isochoric/volumetric decomposition of the deformation and introduces a purely spherical, pointwise non-local deformation gradient together with a bond-level deviatoric deformation gradient. It is worth noting that our approach does not require the use of weak forms or higher-order approximations of the displacement or deformation fields. Instead, it relies on the direct discretization of the classical strong-form integro-differential peridynamic balance equations, employing a meshfree method with standard piecewise-constant approximations of the displacement field. This construction enables a stable one-field, state-based peridynamic formulation that eliminates zero-energy modes and accurately captures the finite deformation behavior of elastic materials with low or negligible compressibility, such as unfilled elastomers and soft biological tissues.

A key feature of the proposed model is its ability to avoid the artificial stiffening effects typically observed in displacement-based finite element models and here shown for standard displacement-based peridynamic correspondence models when the material approaches the incompressible limit. Additionally, the effectiveness of the formulation is independent of the specific compressibility ratio used in the hyperelastic constitutive law, making it broadly applicable within the class of arbitrarily compressible hyperelastic materials. An implicit numerical implementation of the model has also been developed, featuring an analytical definition of the tangent stiffness operator. The resulting non-linear system of equations is solved through a Newton-Raphson iterative procedure, ensuring robustness and computational efficiency in the simulation of large deformation elastic problems. The model has been validated through several illustrative examples involving homogeneous and inhomogeneous finite deformations in isotropic hyperelastic solids, demonstrating both accuracy and stability.

These results enable the extension of peridynamic correspondence models to non-linear problems in nearly incompressible solids potentially involving evolving discontinuities, such as fracture in elastomers and cutting of soft tissues.

CRediT authorship contribution statement

Francesco Scabbia: Writing – review & editing, Writing – original draft, Visualization, Validation, Supervision, Software, Resources, Methodology, Investigation, Formal analysis, Data curation, Conceptualization; **Vito Diana:** Writing – review & editing, Writing – original draft, Visualization, Validation, Supervision, Software, Resources, Project administration, Methodology, Investigation, Funding acquisition, Formal analysis, Data curation, Conceptualization; **Francesca Fantoni:** Writing – review & editing, Writing – original draft, Validation, Supervision, Methodology, Investigation, Funding acquisition, Formal analysis, Conceptualization; **Mirco Zaccariotto:** Writing – review & editing, Validation, Supervision, Methodology, Investigation, Formal analysis, Data curation, Conceptualization; **Ugo Galvanetto:** Writing – review & editing, Validation, Supervision, Resources, Methodology, Investigation, Funding acquisition, Formal analysis, Data curation, Conceptualization.

Data availability

Data will be made available on request.

Declaration of competing interest

The authors declare that they have no known competing financial interests or personal relationships that could have appeared to influence the work reported in this paper.

Acknowledgments

The authors acknowledge support from the European Union - Next GenerationEU under the call PRIN 2022 PNRR of the Italian Minister of University and Research (MUR); Project P2022HLHHB (PE - Physical Sciences and Engineering) *A digital framework for the cutting of soft tissues: A first step towards virtual surgery* (National coordinator V. Diana). F. Fantoni is a member of INdAM-GNFM and gratefully acknowledge the National Group of Mathematical Physics (GNFM-INdAM, Italy). U. Galvanetto acknowledges the financial support of the University of Padova through the project BIRD237212/23 *A soft peridynamic material model to simulate damage and surgery in the brain*.

Funded by the
European Union
NextGenerationEU

References

[1] A. Fassler, C. Majidi, Soft-matter capacitors and inductors for hyperelastic strain sensing and stretchable electronics, Smart Mater. Struct. 22 (5) (2013) 055023.
[2] L. Chen, C. Yang, H. Wang, D.T. Branson, J.S. Dai, R. Kang, Design and modeling of a soft robotic surface with hyperelastic material, Mech. Mach. Theory 130 (2018) 109–122.
[3] H. Ucar, I. Basdogan, Dynamic characterization and modeling of rubber shock absorbers: a comprehensive case study, J. Low Frequency Noise Vib. Active Contr. 37 (3) (2018) 509–518.
[4] S. Budday, T.C. Ovaert, G.A. Holzapfel, P. Steinmann, E. Kuhl, Fifty shades of brain: a review on the mechanical testing and modeling of brain tissue, Arch. Comput. Methods Eng. 27 (2020) 1187–1230.
[5] H.B. Khaniki, M.H. Ghayesh, R. Chin, M. Amabili, Hyperelastic structures: a review on the mechanics and biomechanics, Int. J. Non Linear Mech. 148 (2023) 104275.
[6] S.K. Melly, L. Liu, Y. Liu, J. Leng, A review on material models for isotropic hyperelasticity, Int. J. Mech. Syst. Dyn. 1 (1) (2021) 71–88.
[7] H.B. Khaniki, M.H. Ghayesh, R. Chin, M. Amabili, A review on the nonlinear dynamics of hyperelastic structures, Nonlinear Dyn. 110 (2) (2022) 963–994.
[8] S. Yin, W. Yang, J. Kwon, A. Wat, M.A. Meyers, R.O. Ritchie, Hyperelastic phase-field fracture mechanics modeling of the toughening induced by bouligand structures in natural materials, J. Mech. Phys. Solids 131 (2019) 204–220.
[9] F. Tian, J. Zeng, M. Zhang, L. Li, Mixed displacement–pressure-phase field framework for finite strain fracture of nearly incompressible hyperelastic materials, Comput. Methods Appl. Mech. Eng. 394 (2022) 114933.
[10] F. Tian, J. Zeng, X. Tang, T. Xu, L. Li, A dynamic phase field model with no attenuation of wave speed for rapid fracture instability in hyperelastic materials, Int. J. Solids Struct. 202 (2020) 685–698.
[11] S.A. Silling, Reformulation of elasticity theory for discontinuities and long-range forces, J. Mech. Phys. Solids 48 (1) (2000) 175–209.
[12] S.A. Silling, M. Epton, O. Weckner, J. Xu, E. Askari, Peridynamic states and constitutive modeling, J. Elast. 88 (2) (2007) 151–184.
[13] J. Trageser, P. Seleson, Peridynamics: a tale of two poisson's ratios, J. Peridyn. Nonlocal Model. 2 (2020) 278–288.
[14] V. Diana, Anisotropic continuum-molecular models: a unified framework based on pair potentials for elasticity, fracture and diffusion-type problems, Arch. Comput. Methods Eng. 30 (2023) 1305–1344.
[15] S.A. Silling, F. Bobaru, Peridynamic modeling of membranes and fibers, Int. J. Non Linear Mech. 40 (2–3) (2005) 395–409.
[16] D.J. Bang, E. Madenci, Peridynamic modeling of hyperelastic membrane deformation, J. Eng. Mater. Technol. 139 (3) (2017) 031007.
[17] D.A. Abdoh, A new adaptive peridynamic framework for modeling large deformation and fracture behavior of hyperelastic materials, Eng. Fract. Mech. 314 (2025) 110709.
[18] C. Tamur, S. Li, A bond-based peridynamics modeling of polymeric material fracture under finite deformation, Comput. Methods Appl. Mech. Eng. 414 (2023) 116132.
[19] B.B. Yin, W.K. Sun, Y. Zhang, K.M. Liew, Modeling via peridynamics for large deformation and progressive fracture of hyperelastic materials, Comput. Methods Appl. Mech. Eng. 403 (2023) 115739.
[20] B.B. Yin, W.K. Sun, Y. Zhang, K.M. Liew, Modeling of hyperelastic polymer gels under blunt ballistic impact with three-dimensional flexibilities, Comput. Methods Appl. Mech. Eng. 413 (2023) 116127.
[21] J.C. Bellido, J. Cueto, C. Mora-Corral, Bond-based peridynamics does not converge to hyperelasticity as the horizon goes to zero, J. Elast. 141 (2) (2020) 273–289.
[22] T.L. Warren, S.A. Silling, A. Askari, O. Weckner, M.A. Epton, J. Xu, A non-ordinary state-based peridynamic method to model solid material deformation and fracture, Int. J. Solids Struct. 46 (5) (2009) 1186–1195.
[23] S.F. Henke, Peridynamic modeling and simulation of polymer-nanotube composites (2013). PhD dissertation, Florida State University.
[24] P. Roy, D. Behera, E. Madenci, Peridynamic simulation of finite elastic deformation and rupture in polymers, Eng Fract Mech 236 (2020) 107226.
[25] D. Behera, P. Roy, E. Madenci, Peridynamic correspondence model for finite elastic deformation and rupture in neo-Hookean materials, Int. J. Non Linear Mech. 126 (2020) 103564.
[26] R. Waxman, I. Guven, Implementation of a neoHookean material model in state-based peridynamics to represent nylon bead behavior during high-speed impact, in: AIAA Scitech 2020 Forum, 2020, p. 0725.
[27] W. Yao, X. Zhou, Numerical modelling of compressible hyperelasticity via smoothed state-based peridynamics, Eng. Anal. Bound. Elem. 140 (2022) 476–493.
[28] E. Madenci, P. Roy, D. Behera, Peridynamic modeling of hyperelastic materials, in: Advances in Peridynamics, Springer, 2022, pp. 105–122.
[29] Y. Chen, Y. Yang, Y. Liu, Large deformation and crack propagation analyses of hydrogel by peridynamics, Eng. Fract. Mech. 284 (2023) 109261.
[30] C. Li, H. Zhang, H. Ye, H. Zhang, Y. Zheng, An improved stabilized peridynamic correspondence material model for the crack propagation of nearly incompressible hyperelastic materials, Comput. Methods Appl. Mech. Eng. 404 (2023) 115840.
[31] P. Roy, et al., Peridynamics modeling of cellular elastomeric metamaterials: application to wave isolation, Int. J. Mech. Sci. 254 (2023) 108456.
[32] H.-Y. Liu, L.-C. Qiu, Y. Liu, Non-ordinary state-based peridynamic simulation of compressive large deformation and failure in hydrogel materials, Extreme Mech. Lett. (2025) 102348.
[33] T. Breitzman, K. Dayal, Bond-level deformation gradients and energy averaging in peridynamics, J. Mech. Phys. Solids 110 (2018) 192–204.
[34] M.S. Breitenfeld, P.H. Geubelle, O. Weckner, S.A. Silling, Non-ordinary state-based peridynamic analysis of stationary crack problems, Comput. Methods Appl. Mech. Eng. 272 (2014) 233–250.
[35] M.R. Tupek, R. Radovitzky, An extended constitutive correspondence formulation of peridynamics based on nonlinear bond-strain measures, J. Mech. Phys. Solids 65 (2014) 82–92.
[36] J.T. Foster, X. Xu, A generalized, ordinary, finite deformation constitutive correspondence model for peridynamics, Int. J. Solids Struct. (2018).
[37] M. Behzadinasab, J.T. Foster, On the stability of the generalized, finite deformation correspondence model of peridynamics, Int. J. Solids Struct. 182 (2020) 64–76.
[38] D.J. Littlewood, Simulation of dynamic fracture using peridynamics, finite element modeling, and contact, in: ASME International Mechanical Engineering Congress and Exposition, 44465, 2010, pp. 209–217.
[39] S.A. Silling, Stability of peridynamic correspondence material models and their particle discretizations, Comput. Methods Appl. Mech. Eng. 322 (2017) 42–57.
[40] H. Chen, Bond-associated deformation gradients for peridynamic correspondence model, Mech. Res. Commun. 90 (2018) 34–41.
[41] F. Bobaru, J.T. Foster, P.H. Geubelle, S.A. Silling, Handbook of peridynamic modeling, Adv. Appl. Math. CRC Press (2015).
[42] T.J.R. Hughes, The finite element method: linear static and dynamic finite element analysis, Courier Corpor. (2012).
[43] T. Bode, C. Weißenfels, P. Wriggers, Mixed peridynamic formulations for compressible and incompressible finite deformations, Comput. Mech. 65 (5) (2020) 1365–1376.
[44] S.A. Silling, E. Askari, A meshfree method based on the peridynamic model of solid mechanics, Comput. Struct. 83 (17–18) (2005) 1526–1535.
[45] H. Chen, B.W. Spencer, Peridynamic bond-associated correspondence model: stability and convergence properties, Int. J. Numer. Methods Eng. 117 (6) (2019) 713–727.
[46] G.A. Holzapfel, Nonlinear Solid Mechanics: A Continuum Approach for Engineering Science, Kluwer Academic Publishers Dordrecht, 2002.

[47] C. Truesdell, W. Noll, C. Truesdell, W. Noll, The Non-Linear Field Theories of Mechanics, Springer, 2004.
[48] E.A. de Souza Neto, D. Peric, D.R.J. Owen, Computational Methods for Plasticity: Theory and Applications, John Wiley & Sons, 2011.
[49] ABAQUS/Standard User's Manual, Version 6.9, Simulia, 2009.
[50] U. Brink, E. Stein, On some mixed finite element methods for incompressible and nearly incompressible finite elasticity, Comput. Mech. 19 (1) (1996) 105–119.
[51] R. De Borst, M.A. Crisfield, J.J.C. Remmers, C.V. Verhoosel, Nonlinear Finite Element Analysis of Solids and Structures, John Wiley & Sons, 2012.
[52] M.A. Crisfield, Non-linear Finite Element Analysis of Solids and Structures. Volume 2: Advanced Topics, Chichester: John Wiley & Sons, 1997.
[53] P. Wriggers, Computational Contact Mechanics, Springer Verlag, Berlin, Heidelberg, 2006.
[54] P. Van den Bogert, R. De Borst, G.T. Luiten, J. Zeilmaker, Robust finite elements for 3D-analysis of rubber-like materials, Eng. Comput. 8 (1) (1991) 3–17.
[55] P. Van den Bogert, R. De Borst, On the behaviour of rubberlike materials in compression and shear, Arch. Appl. Mech. 64 (2) (1994) 136–146.
[56] P. Le Tallec, Numerical methods for nonlinear three-dimensional elasticity, Handbook Numer. Anal. 3 (1994) 465–622.
[57] T. Sussman, K.-J. Bathe, A finite element formulation for nonlinear incompressible elastic and inelastic analysis, Comput. Struct. 26 (1–2) (1987) 357–409.
[58] D.J. Littlewood, Roadmap for Peridynamic Software Implementation, Technical Report, Sandia National Lab.(SNL-NM), Albuquerque, NM (United States), 2015.
[59] F.S. Vieira, A.L. Araújo, On the role of bond-associated stabilization and discretization on deformation and fracture in non-ordinary state-based peridynamics, Eng. Fract. Mech. 270 (2022) 108557.
[60] F. Scabbia, M. Zaccariotto, U. Galvanetto, Accurate computation of partial volumes in 3D peridynamics, Eng. Comput. 39 (1) (2023) 959–991.
[61] J.-C. Simo, F. Armero, Geometrically non-linear enhanced strain mixed methods and the method of incompatible modes, Int. J. Numer. Methods Eng. 33 (7) (1992) 1413–1449.
[62] M. Hillman, M. Pasetto, G. Zhou, Generalized reproducing kernel peridynamics: unification of local and non-local meshfree methods, non-local derivative operations, and an arbitrary-order state-based peridynamic formulation, Comput. Part. Mech. 7 (2) (2020) 435–469.
[63] M. Pasetto, Y. Leng, J.-S. Chen, J.T. Foster, P. Seleson, A reproducing kernel enhanced approach for peridynamic solutions, Comput. Methods Appl. Mech. Eng. 340 (2018) 1044–1078.
[64] T. Bode, C. Weißenfels, P. Wriggers, Peridynamic petrov-galerkin method: a generalization of the peridynamic theory of correspondence materials, Comput. Methods Appl. Mech. Eng. 358 (2020) 112636.
[65] T. Bode, C. Weißenfels, P. Wriggers, A consistent peridynamic formulation for arbitrary particle distributions, Comput. Methods Appl. Mech. Eng. 374 (2021) 113605.
[66] T. Bode, C. Weißenfels, P. Wriggers, Peridynamic galerkin method: an attractive alternative to finite elements, Comput. Mech. 70 (4) (2022) 723–743.
[67] E. Madenci, A. Barut, M. Dorduncu, Peridynamic Differential Operator for Numerical Analysis, 10, Springer, 2019.
[68] M.S. Breitenfeld, P.H. Geubelle, O. Weckner, S. Silling, Non-ordinary state-based peridynamic analysis of stationary crack problems, Comput. Methods Appl. Mech. Eng. 272 (2014) 233–250.
[69] R. Ogden, Non-Linear Elastic Deformations, Courier Corporation, 1997.
[70] J. Schröder, T. Wick, S. Reese, P. Wriggers, R. Müller, S. Kollmannsberger, M. Kästner, A. Schwarz, M. Igelbüscher, N. Viebahn, et al., A selection of benchmark problems in solid mechanics and applied mathematics, Arch. Comput. Methods Eng. 28 (2021) 713–751.
[71] M.J. Buehler, H. Gao, Dynamical fracture instabilities due to local hyperelasticity at crack tips, Nature 439 (7074) (2006) 307–310.
[72] R. Hassani, R. Ansari, H. Rouhi, Large deformation analysis of 2D hyperelastic bodies based on the compressible nonlinear elasticity: a numerical variational method, Int. J. Non Linear Mech. 116 (2019) 39–54.
[73] A. Pagani, P. Chiaia, M. Filippi, M. Cinefra, Unified three-dimensional finite elements for large strain analysis of compressible and nearly incompressible solids, Mech. Adv. Mater. Struct. 31 (1) (2024) 117–137.